Surface structure, activity and microgravimetry modeling delineate contrasted mud chamber types below flat and conical mud volcanoes from Azerbaijan

Francis Odonne, Patrice Imbert, Dominique Remy, Germinal Gabalda, Adil Aliyev, Orhan Abbasov, Elnur Baloglanov, Victoria Bichaud, Remy Juste, Matthieu Dupuis, et al.

Surface structure, activity and microgravimetry modeling delineate contrasted mud chamber types below flat and conical mud volcanoes from Azerbaijan.

Francis Odonne[1], Patrice Imbert[2], Dominique Remy[1], Germinal Gabalda[1], Adil A. Aliyev[3], Orhan R. Abbasov[3], Elnur E. Baloglanov[3], Victoria Bichaud[1], Remy Juste[1], Matthieu Dupuis[4],

1 : Géosciences Environnement Toulouse (GET), Observatoire Midi Pyrénées, Université de Toulouse, CNRS, IRD, UMR 5563, 14 Avenue E. Belin, F31400 Toulouse, France.

2 : Laboratoire des Fluides Complexes et de leurs Réservoirs (LFCR), Université de Pau et des Pays de l'Adour, Avenue de l'Université, F64000 Pau Cedex, France.

3 : Institute of Geology and Geophysics, Azerbaijan National Academy of Sciences, H. Javid Avenue, 119, Baku AZ1143, Azerbaijan.

4 : Univ. Lille, CNRS, Univ. Littoral Côte d'Opale, UMR 8187, LOG, Laboratoire d'Océanologie et de Géosciences, F 59000 Lille, France.

Abstract

We compared the structure of two flat and two conical mud volcanoes (MV) in Azerbaijan in order to understand what governs the morphological contrast. We paid particular attention to the structural evolution of the surface, as observed in the field over 5 years and as monitored by satellite images revealing surface activity over that period; in addition, we acquired microgravity measurements to probe deeper structure. The combination of these data reveals in all studied volcanoes significant mass deficit concentric with the surface edifice. Modeling indicates that the mass deficit is consistent with a chamber underlying the summit caldera of conical MVs and the plateau of flat MVs, with a thickness of several hundred meters for a density contrast of 500 kg/m^3 between the chamber mud and the surrounding solid

mud. Surface structures and their evolution during and in between eruptions provide insight into the depth of the mud chamber, which lies within a few meters of the surface for flat mud volcanoes and one to several hundred meters deep for conical ones. Surface structures and satellite-derived deformation analysis shows that flat mud volcanoes grow by radial expansion and compression of the flanks distributed all around the edifice. In contrast, conical mud volcanoes grow by flow stacking in the summit caldera, deformation being constrained by the caldera rim; excess mud supply is accommodated by occasional rim breaching and mud overflow into flank gullies.

Keywords: mud-volcano-structure; mud-chamber; mud-volcano-growth-processes; conical-mud-volcano; mud-pie; microgravimetry; InSAR-data.

1. Introduction

Mud volcanoes are common geological features in areas undergoing high sedimentation rates, in particular where they are affected by compressive tectonics (Higgins and Saunders, 1974; Henry et al., 1990; Kopf, 2002; Deville et al., 2003). Mud volcanoes are characterized by the emission of mud to the surface of the Earth or to the seabed, generally at temperature close to ambient (Guliev and Feizullayev, 1996; Planke et al., 2003; Feseker et al., 2009). Mud is generally emitted steadily at low rates (m^3 per year) through small (m-size) outlets called gryphons during phases of quiescence, and episodically with high rates (thousands to millions of m^3 in one day) during eruptions that occasionally go along with large volume bursts of methane gas and emission of fountains of mud. The products of eruptions stack over time to build up edifices, some of which reach diameters of several kilometers and heights of several hundred meters. The corresponding deposits typically consist of a mixture of polygenic clasts, dominantly shaly, floating in a homogeneous mud matrix. They are known as “mud breccia” (Cita et al., 1981).

The morphology of mud volcanoes is overall well known, offshore from bathymetric surveys and onshore by field studies (Le Pichon et al., 1990; Lance et al., 1998; Deville et al., 2003; Loncke et

al., 2004; Dupré et al., 2008). They are organized in a continuum between regular conical and flat edifices, the latter group being called “mud pies” (Loncke et al. 2004; Yusifov and Rabinowitz, 2004; Mazzini and Etiope, 2017). A conventional value of 5° on the surface gradient was set by Kopf (2002) as the limit between mud cones and mud pies. Mazzini and Etiope (2017) proposed a classification of mud volcanoes into 12 types based on their surface morphology. They describe a continuum ranging from the flattest edifices, which they call “plateau-like” to high-positive-relief cones and negative relief “sinkhole-type”. In contrast to this high level of detail regarding the surface, the feeding system depicted by the authors for the 12 types appears rather idealized, with a vertical conduit sharply widening close to the surface, superimposed onto subsurface structures that indicate compression for 9 types and localized subsidence for the other 3. We felt that this unique subsurface architecture may not be enough to account for the great variety of surface manifestations and terrain structures and suspected a possible link between the shape of mud volcanoes and their feeding system.

Numerous investigations have sought to define the deep structure of mud volcanoes, the main lines of research being into the architecture of deep piping and conduits conveying fluids (Davies and Stewart, 2005; Dupuis et al., 2019; Mazzini et al., 2008; Roberts et al., 2010; Kirkham et al., 2017, Kopf and Behrmann, 2000), the reality of existence and position at depth of a mud chamber (Deville et al., 2003; Rudolph et al., 2011; Dupuis et al., 2019; Menapace et al., 2019) as well as the interpretation of 2D or 3D seismic images of mud volcanoes (Yusifov and Rabinowitz, 2004; Praeg et al., 2009; Dupuis et al., 2019) and the use of gravity measurements (Kadirov and Mukhtarov, 2004; Feyzullayev et al., 2005).

The notion of “mud chamber” implies the existence prior to the eruption of a volume of fluid mud at depth, likely homogenized, ready for remobilization. The existence of mud chambers has been postulated but without direct evidence so far for the existence at any time of a large body of fluid mud in the subsurface. A subsurface body of mud breccia in Trinidad delineated by borehole correlation has been interpreted as a fossil mud chamber by Deville et al. (2003), but an alternative interpretation as a stack of fossil mud volcanoes has been proposed from the same dataset by Stewart and Davies (2006).

In contrast, the concept of "depletion zone" was derived from seismic interpretation to account for the fact that the volume of mud emitted to the surface as a mud volcano balances out with the removal at depth of an equivalent volume whose outline can be defined, either in map view (Stewart and Davies, 2006) or in 3D (Kirkham et al., 2017; Dupuis et al., 2019). Structurally restoring a depletion zone is a way of defining the outline of the source volume of the mud below a mud volcano from clear geometric relationships, without the difficulties related to interpreting seismic in zones of reflection-free or chaotic seismic signal. However, observing a depletion zone does not make it possible to decide whether the erupted mud belonged to a preexisting chamber of low-strength mud prior to erupting, or just formed in subsurface progressively as the eruption proceeded. In the latter hypothesis, modeled from the LUSI eruption (Karyono et al., 2017), mud breccia starts forming from subsurface stratified sediment as the initiation of fluid release changes pressure conditions at depth, resulting in dissolved methane exsolution and sediment liquefaction / loss of strength (Blouin et al. 2020). LUSI is interpreted to follow this "no-chamber" model, leaving the existence of mud chambers an unresolved issue.

We investigated the structure of four active mud volcano systems of Azerbaijan (i.e. integrating the surface mud volcano proper and subsurface elements), selected to exemplify both main morphological types, i.e. flat and conical edifices. Our field investigations were focused on surface structural elements in the mud breccia of the volcanic edifices (active or recent faults, fractures, folds, etc.) and their evolution over the years, in order to better constrain the processes that lead to formation of pie-like mudflows, deformation of summit collapse caldera, or overspill of radial mudflows. These surface elements and manifestations are related to activity of the mud volcano itself (Hovland et al. 1997; Antonielli et al., 2014; Iio and Furuya, 2018; Dupuis et al., 2019; Odonne et al., 2020), to the response of the deep plumbing system to the tectonic stress regime (Stewart and Davies, 2006; Mazzini et al., 2007; Manga et al., 2009; Roberts et al., 2010; Bonini et al., 2016; Maestrelli et al., 2017; Maestro et al., 2019) or tectonic activity (Menapace et al., 2017) and also depend on the plumbing system of the mud volcano reacting to the regional tectonic deformation field (Fowler et al., 2000; Viola et al., 2005;

Mellors et al., 2007; Praeg et al. 2009; Bonini and Mazzarini, 2010; Forte et al., 2010; Somoza et al., 2012; Bonini, 2012; Kadirov et al., 2014).

We therefore propose to study here how the subsurface structure of a mud volcano and the mud supply system influence the type of surface buildup. For this we followed the evolution of 4 active Azerbaijan mud volcanoes, two of each type, combining (1) field observations and structural measurements carried out over a span of 6 years with (2) the interpretation of InSAR data recorded over the same period and (3) the modelling of microgravity measurements we acquired during our field campaigns.

2. Geological setting

The study area in Azerbaijan belongs to the foothills of the SE termination of the Greater Caucasus Range, as evidenced by the stratigraphic and structural trends visible on geological maps (Fig. 1b). The structural axes are the surface expression of the collision that led to the build-up of the Greater Caucasus Range and flexural subsidence of the South Caspian Basin (Dercourt et al., 1986; Devlin et al., 1999; Roberts et al., 2011). The closure of the Paratethys ocean from the middle Miocene onwards resulted in the formation of NW-SE oriented folds and in the bending of the Arabian plate under the Eurasian plate (Brunet et al., 2003). The South Caspian Basin is characterized by rapid subsidence and a very high sedimentation rate, both up to 2.5 km / My during the Pleistocene (Yusifov and Rabinowitz, 2004; Vincent et al., 2005; Smith-Rouch, 2006). Sediments have been provided to the basin by the Volga, the Kura and the paleo-Amu Darya Rivers, respectively draining the Russian craton to the north, the Caucasus Ranges to the west and the Hindu Kush, Pamir and Kopet Dagh to the east and south (Fig. 1b, inset). The northern part of Azerbaijan is structured parallel to the Absheron ridge which is the extension of the Greater Caucasus into the Caspian Sea. Measurements of present-day ground displacement by GNSS measurements (Global Navigation Satellite System, including GPS data) also make it possible to determine the active compression directions. They confirm that the compression towards the NNE at the

129 origin of the anticlines of Azerbaijan continues today in the same direction (Forte et al., 2010; Bonini
130 and Mazzarini, 2010; Kadirov et al., 2012, 2014).

131 The regional stratigraphy is summarized in Fig. 1c. Oligo-Miocene organic-matter-rich
132 Maykop and Diatom Formations reached oil and gas-generating depths during the Neogene in the study
133 area and are currently expelling hydrocarbons, leading to oil and/or gas accumulation in anticlines,
134 onshore and offshore. At the same time, very high sedimentation rates resulted in shale under-
135 compaction, high overpressures and low temperature gradients in the most subsiding areas. The
136 reservoirs are fluvio-deltaic sandbodies of the Mio-Pliocene "Productive Series" Suite alternating with
137 overpressured shales (Javanshir et al., 2015; Blouin et al., 2019). Both active gas migration and high
138 overpressure conditions promote the activity onshore Azerbaijan of >300 mud volcanoes that constantly
139 release methane and brine through their gryphons and occasionally expel large amounts of mud and
140 hydrocarbons during eruptions (Jakubov et al., 1971; Fowler et al., 2000; Stewart and Davies, 2006;
141 Aliev et al., 2015). Stratigraphic analysis of the clasts of the mud breccia indicates the Oligo-Miocene
142 Maykop formation as being the main mud source (Inan et al., 1997; Dimitrov, 2002). The location of
143 mud volcanoes onshore and offshore is strongly controlled by the structure, with most mud volcanoes
144 located above anticline crests, as summarized in Bonini and Mazzarini (2010, their Fig. 1).
145

146 ## 3. Methods

147 3. 1. Field data

148 The selected conical mud volcanoes have reliefs of several hundred meters above the surrounding plains,
149 while the flat volcanoes have reliefs of a few tens of meters only (Fig. 2). We investigated in detail two
150 flat (namely the Ayazakhtarma mud volcano: Ayazakhtarma MV and the Akhtarma-Pashaly mud
151 volcano: Akhtarma-Pashaly MV) and two conical mud volcanoes (namely the Toragay mud volcano:
152 Toragay MV and the Otmanbozdag mud volcano: Otmanbozdag MV) during six field missions between
153 2014 and 2019. Field work combined detailed mapping of structural and morphological features at the
154 surface of the mud volcanoes, as shown in Odonne et al. (2020) and the estimation of local variations in

topography and relative directions of movement between successive field work sessions. These field surveys were compared with photomosaics taken during drone overflights. We used a DJI Mavic-Pro, which we flew at heights between 30 and 500 m. The reconstructed photomosaics were compared with SPOT7 and Pléiades satellite images to trace active structures and displacement fields (Odonne et al., 2020).

3. 2. InSAR data and satellite-derived topography

SAR imagery over the study area was acquired by two satellite missions: C-band Interferometric Wide Swath mode images from the European Space Agency (ESA) Sentinel-1A/B and L-band Stripmap mode images from ALOS 2 operated by the Japan Aerospace Exploration Agency (JAXA). The wavelengths for C-band and L-band are 6 and 24 cm, respectively. The C-band SAR dataset used in this study includes 59 acquisitions from ascending orbits (6 October 2014 to January 2017) and 28 acquisitions from descending orbits (23 October 2014 to 23 March 2017). The L-band SAR dataset is composed of 8 ALOS-2 images: 5 from ascending orbits (11 August 2017 to 23 October 2019) and 3 from descending orbits (31 May 2017 to 29 May 2019). We used the ISCE software (Rosen et al., 2012) to generate interferograms using the two-pass method described by Massonnet and Feigl, (1998). These were next filtered using a weighted power spectral density filter and some of them were unwrapped using an implementation of the Statistical cost, Network flow Algorithm for PHase Unwrapping -SNAPHU (Chen and Zebker, 2002). Two-dimensional displacement maps (easting and vertical components of the displacement) presented in this study were computed using the approach proposed by Wright et al. (2004).

In order to assess the topographic evolution of the Otmanbozdag MV during the Sept. 2018 eruption, we compared elevation data we measured at each individual station during the gravimetry acquisition with the digital elevation model (DEM) AW3D30 (JAXA, 2015). The expected vertical accuracy of AW3D30 is given to be better than 5 m of Root Mean Square Error (RMSE) (Tadono et al., 2016). We calibrated AW3D30 against our GNSS measurements using 66 Ground Control Points

distributed over the whole study area, excluding the zones of active volcanism. This comparison yields an average error of 0.90 m and RMSE of 2.54 m, knowing that the spatial sampling of AWD3D30 is 30 m, compared to the pinpoint positioning of GNSS measurements.

3. 3. Gravity measurements

The gravity data used in this study were acquired during two field campaigns carried out in May 2018 and 2019, respectively. In 2018, gravity data were collected at the Ayazakhtarma MV. During the second field campaign, we improved the gravity network geometries at the mud volcanoes visited the previous year, and we acquired gravity data at the Akhtarma-Pashaly MV, Otmanbozdag MV and Toragay MV. The gravity measurements were performed using SCINTREX CG5 (2018) and CG6 (2019) relative gravimeters and for each mud volcano we revisited some sites in order to control and remove the instrumental drift (See Fig. 7 for the location of the microgravity measurements carried out during 2018 and 2019 field surveys).

Both SCINTREX instruments (CG6 SN#18100125 and CG5 SN#9424) have been calibrated using a calibration line established with an absolute gravimeter (Micro-g LaCoste A10 #014) by the International Gravimetric Bureau (BGI) and the French Geographic Institute (IGN) between our laboratory in Toulouse and l'Hospitalet-près-Andorre (Δh=1290m and Δg=445 mGal). The agreement of both instruments has been confirmed from the measurements performed on the Ayazakhtarma MV. The overall accuracy of the gravity measurements during the field surveys is estimated to be within 0.020 mGal.

All the positions of the gravity stations were determined by differential GNSS measurements using dual-frequency receivers (Topcon® GB-1000 in May 2018 and Leica® GR25 in May 2019). We installed a permanent base station to locate the rover station usually less than 5 km. The GNSS data were analyzed with the GINS software package developed by the French National Centre for Space Studies (CNES), using a Precise Point Positioning (PPP) technique (Marty et al., 2011) and RTKLIB,

the package for GNSS Positioning. The coordinates of the gravity stations are estimated to be achieved with an accuracy better than 10 cm for both horizontal and vertical components.

We used the CG5TOOL (Gabalda et al., 2003) to calculate the Free Air and the Complete Bouguer anomalies. We used 0.3086 mGal/m for the free-air correction and we assumed a density value of 2.67 for the terrain corrections calculated with GRAVSOFT algorithm (Tscherning et al, 1992). No regional corrections were applied to the gravity data collected on the conical mud volcanoes. In contrast, we applied a regional linear correction to the Ayazakhtarma MV and Akhtarma-Pashaly MV Bouguer anomalies for their clear gravity trends, respectively NW-SE and a SW-NE, thereby highlighting shallow density contrasts beneath these mud volcanoes. We interpolated the Bouguer anomaly values using a least-square collocation method to produce the Bouguer anomaly fields. A constant standard deviation of 0.05 mGal for the gravity anomalies is considered further.

For all the surveyed mud volcanoes, we followed the strategy explained by Odonne et al. (2020) to invert gravity data, as follows: we first created a 3-D mesh to build the kernel that maps from the physical parameter space to the data space, and then used the following data misfit to measure the goodness of the fit between the observed and the modeled data:

$$\emptyset_d(\mathbf{m}) = \|W_d\ (G(\mathbf{m}) - \mathbf{d}_{obs})\|_2^2 \qquad (1)$$

where Wd is a diagonal matrix with Wdii elements being equal to the inverse of the standard deviation of the ith gravity observations and G the kernel next, we minimized the following global objective function using the scaled iterative reweighted least square optimization approach proposed by Fournier et al (2016) and Miller et al. (2017):

$$\emptyset(\mathbf{m}) = \emptyset_d(\mathbf{m}) + \beta\emptyset_m(\mathbf{m}) \qquad (2)$$

where $\emptyset_d(\boldsymbol{m})$ is the data misfit, $\emptyset_m(\boldsymbol{m})$ is the stabilizing regularization and β the Tikhonov parameter. We performed an optimization using a two-step inversion approach, first by inverting the data with a "smooth" constraint (*i.e.*, β not too small) and next by compacting the resulting smooth model using a norm L_p, where $0<<L_p<<2$. Inversion of gravity data is a strongly underdetermined problem (more

unknowns that equations), so that it is necessary to make simplifying hypotheses on parameters that cannot be determined from other sources of information. We thus searched for the most compact body located beneath the mud volcanoes by fixing a lower density contrast bound to 500 kg/m^3 and incorporating depth weighting. The best models presented hereafter are the most compact and deepest sources that are able to properly match the observed gravity data for a given mud volcano.

4. Results

4. 1. Otmanbozdag mud volcano

The Otmanbozdag MV has been regularly active over the past 160 years with 10 eruptions recorded since 1854 (Aliyev et al., 2019). It is the only mud volcano of Azerbaijan onshore on which an eruption resulting in a long-distance mud overflow occurred recently enough to be documented by public domain high-resolution satellite pictures. This recent eruption, the latest to date, occurred on Sept. 23, 2018. It generated a mudflow that overspilled the crater through a breach on the S side and branched out into the preexisting network of gullies on the flanks; the longest branch ends on the coastal plain, 2.9 km from the emission center. Figure 3a is a mosaic of drone photos taken in May 2019. It shows the deformation of the central part of the flat top of the mud volcano, mainly resulting from the 2018 eruption. It also shows the upper part of the southward flows. A photo taken on Sept. 23, 2018 shows gas burning in the crater at the end of this eruption (Fig. 3b).

The top part of the Otmanbozdag MV in its post-eruption configuration (Fig. 4) shows an approximately concentric structure centered on what appears as the main emission point of the recent flow (point C in Fig. 3a), a peripheral rim partially covered with vegetation surrounding a 700-m-diameter scarcely vegetated central area on which two overlapping patches of gray mud, 150-200 m in diameter each, are totally devoid of vegetation. The northern side is affected by a double radial deformation marked by compression and extension (Fig. 4a). The compressive deformation is the most external, it shows that the central part was locally thrusted over the outer vegetated moat. All the areas

256 inside are marked by radial extension with tension fractures several meters wide (Fig. 4a) and up to 10 m
257 deep.

258 The central part recorded concentric deformation exemplified by a transect from the W
259 margin to the center in Fig. 4b. The marginal part shows extensive deformation with small, tilted blocks
260 arranged concentrically and progressively passing to diamond-shaped blocks. These are bounded by
261 tension fractures which indicate two directions of extension: one radial, centered on point C and the
262 other trending southward and related to recent mudflows. Finally, the most central part is affected by
263 extensive deformation that cuts blocks into prismatic columns between which relatively protected rafts
264 remain, with a relief of ca. 0.5 m (Fig. 4b). The area of overflow (Fig. 3a) shows a complete collapse of
265 the edge of the mud volcano with many blocks tilted towards the flow (Fig. 4c). Lateral sliding surfaces
266 of the crater breach wall commonly show a double system of mechanical grooves: at the top of the
267 surfaces the grooves are horizontal and parallel to the main flow direction (fracture 125N dipping 32°NE
268 with right lateral horizontal striae) while in the lower part the grooves are oblique, pointing down away
269 from the volcano center. They show a combination of normal and strike slip displacements (fracture
270 125N, dip 32°NE with striae 70N dipping 30°E indicating both normal and right lateral displacements).

271 A first insight into the deformation undergone by the Otmanbozdag MV crater during the Sept.
272 2018 eruption can be obtained by comparing the AW3D30 DEM, acquired in 2015, with elevations
273 measured by GNSS during our microgravimetry acquisition in May 2019 (Fig. 5). The pre-eruption
274 topography shows a regular dome in the crater, with in the central part a 30-m relief above the moat that
275 follows the inner part of the crater rim. In contrast, the post-eruption topography is flat at 373 m +/- 1 m
276 over a 600-m-diameter zone. The altitude is approximately that of the points measured on the crater rim,
277 and about 8 m above the moat that separates the rim from the center. Overall, the eruption flattened a
278 preexisting dome by a maximum of 15 m in the center, i.e., clearly greater than the confidence domain
279 of the measurements.

280 Satellite Radar interferometry makes it possible to access a shorter period of time and obtain a
281 much higher spatial resolution. The 12-day revisit time of Sentinel-1A/B allows for the recognition of

different patterns of ground displacements observed during the two-year period of observation (Fig.6). In the year preceding the eruption (Fig. 6a) a constant short wavelength interferometric signal is observed by InSAR within the crater, indicating that the activity is concentrated in this area. This area generally shows low coherence values impeding to derive reliable phase estimates. Nevertheless, some coherent interferograms capture a subsidence pattern restricted to the summit (Fig. 6a-1). In the weeks preceding the eruption, at the end of August 2018 (Fig. 6a-2), the active zone gradually widened towards the SE sector of the summit. Examination of satellite pictures over the two years preceding the eruption indicates that this activity corresponds to the progressive SE-ward translation of a 100-m-wide, 500-m-long block limited by strike-slip faults and extending from the central part of the crater into the upper part of a gully on the flank of the Otmanbozdag MV. Interferograms built over periods of 12 days around the Sept. 2018 eruption indicate a high level of deformation all over the summit and extending into the southern breach (Fig. 6c). After the eruption (Fig. 6b), ground displacement mainly occurred within the crater rim and over the distal tips of the flows. In order to attempt deciphering the process that caused the strong interferometric signal captured in the interferograms encompassing the eruption, we went deeper into the InSAR analysis using images acquired by ALOS-2 satellite. ALOS-2 data cover a longer time span (6 and 12 months, respectively) than Sentinel-1 data. Nevertheless, the analysis of the long Sentinel-1 InSAR time series confirms without ambiguity that the observed ground displacement captured by ALOS is mainly induced by the transient processes that occurred in September 2018.

The observed interferometric signal is complex and can be separated into two main signals (Fig. 6c): an incoherent signal affecting the central part of the mud volcano roughly delimited by the crater rim and a subsidence extending beyond the central part. The origin of this loss of coherence within the crater is mainly due to strong displacements triggered by the collapse of the summit part of the mud volcano. The upper part of the mud volcano flank experienced strong deformation causing strong aliasing of the phase. Due to 4 times longer wavelength of L- compared to C-band, the extent of the area affected by this strong aliasing in ALOS-2 interferograms is lower than in Sentinel-1 interferograms (Fig. 6c). We combined ascending and descending ALOS tracks to retrieve the vertical and the easting

components of ground displacement to map the displacement field at the Otmanbozdag MV (Fig. 6d). The easting displacement map exhibits a double-lobe pattern with a positive lobe pattern (displacement toward the east) equal to the negative one (displacement toward the west). Coherent subsidence could be calculated up to 12 cm (half-wavelength), while maximum easting displacements is about 7 cm, westward on the eastern side and eastward on the western side (about quarter-wavelength), indicating trapdoor-like convergence from the two sides. The incoherent signal affecting the central part of the mud volcano makes it impossible to reliably estimate the subsidence of the caldera from InSAR only.

Microgravimetry measurements indicate that the Otmanbozdag MV is characterized by a negative Bouguer gravity anomaly of -3 mGal of small horizontal extent, ca. 500 m, (Fig. 7a, Otmanbozdag). The small spatial extent of the gravimetry network on this conical mud volcano makes it possible to decipher only short-scale spatial density heterogeneities in the shallow part of the edifice. Nevertheless, it seems that the anomaly wavelength lies between the diameters of the summit crater and the base of the mud volcano. This indicates that the observed anomalies would be related to shallow source located within the mud volcanic edifice. Gravity inversion shows that a small compact source with a mass deficit of 2.1×10^{10} kg located at depth of about 150 m beneath the upper part of the mud volcano is able to well explain the gravity data, leading to a root mean square (rms) of the residuals between the observed and the modeled data of 0.031 mGal (Fig. 8.a).

4. 2. Toragay mud volcano

The Toragay is a large constructional mud cone, one of the tallest among the mud volcanoes of Azerbaijan. It dominates the surrounding plain by 300 m (Fig. 1a-b, Fig. 9 a). Two eruptions occurred on March 1 and April 22, 2018 after 30 years of inactivity (Aliyev et al., 2019), the latter produced two separate pie-like mudflows. Figure 9b is a mosaic of drone photos taken in May 2018, it shows the flat top as well as the April 2018 mudflow that spilled over the crater rim down into a slope gully on the west flank. Figure 9c presents drone images of the flat top of Toragay, the drawing of the 2018 pie-like mudflows and the 400-m diameter caldera at the top. At least seven pie-like mudflows are exposed in

the crater, the last three dated from March and April 2018 and the others emplaced before 1988 according to historical records (Aliyev et al., 2019). Mud bomb impacts are scattered over all three recent mudflows and sinter mounds / patches (zones of burned ground, cf. Hovland et al., 1997) have been observed on both April 22 mudflows. The faulted rim of the caldera blocked the northward effusion of the pie-like mudflows (Fig. 9c-2) but the eastern edge of the eastern mudflow extended beyond the caldera rim fault before subsiding along with the floor (Fig. 9c-4). Collapse subsidence is evidenced by sub-vertical striae marked in the fresh mud along the rim fault (Fig. 9c-5). On the western side, a 20 m x 40 m block at the edge of the caldera was pushed and compressed westwards by the pie-like mudflow which eventually bypassed the block and flowed over the rim (Fig. 9b and 9c-3) into a slope gully.

InSAR time series of the Toragay MV are characterized by an interferometric signal confined within the caldera, a clear indication that deformation is strictly limited to the top part of the volcano during eruptions of March and April 2018. Unfortunately, the low spatial resolution of Sentinel-1 SAR data and the loss of coherence generally precludes obtaining a clear image of ground displacement field (Fig.10). Co-eruptive interferograms exhibit low coherence within the crater which is probably due to the emplacement of mud flows that caused a complete loss of phase coherence. Post-eruptive interferograms show concentric ground displacement patterns centered on the 2018 pie-like mudflows, likely related to their progressive contraction through desiccation. As far as we can see, the eruptions were not preceded by large wavelength ground displacement.

The Toragay MV is characterized by a negative Bouguer gravity anomaly of –1.5 mGal over a 300-m-diameter central zone (Fig.7a, Toragay). This value is about 3 times smaller than the one observed at the Otmanbozdag MV. Like at the Otmanbozdag MV, the anomaly wavelength lies between the diameters of the summit crater and the base of the mud volcano, suggesting the presence of a shallow source located within the mud volcanic edifice. Gravity inversion yields a small compact source with a mass deficit of 0.59×10^{10} kg located at a depth of about 300 m beneath the mud volcano crater. This model is able to properly match the gravity data leading to a residual between the observed and the modeled data of 0.018 mGal (Fig.8a).

360

361 4. 3. Akhtarma-Pashaly mud volcano

362 The Akhtarma-Pashaly MV is a large flat-topped mud volcano dominating the Kura plain by
363 almost 300 m (Fig. 1a-b, Fig. 11a). The mud volcano is located on the edge of the Caucasus frontal
364 thrust (Forte et al., 2010), which brought the volcanic plateau to this altitude. The morphology of the
365 western-southwestern outer slope of the Akhtarma-Pashaly MV shows two parts, a ~ 6 km-radius lower
366 part dominated by mudflow deposition with a slope of ca. 2° and a 400-500 m-radius upper part
367 dissected by deep gullies with a slope of 8-10 ° (Fig. 11b and 11c). A similar dual-gradient apron is
368 present on the NE side. The volcanic apparatus does not seem to exceed a thickness of a hundred meters
369 (Fig 12a). Recent activity of the Akhtarma-Pashaly MV is concentrated on four mud pies scattered over
370 the plateau, the central and eastern mud pies having been the most active in the past 10 years (Odonne
371 et al., 2020; Fig. 12b). Pies whose recent activity could be documented grew by emission of mud and
372 bombs from a central vent during discrete episodes. The central mud pie (Fig. 12c) underwent two mud
373 eruptions in 2017 and 2018, which both deformed the last underlying pre-2017 mudflow. Radial
374 spreading of a pie during mud emission induced deformation by compressive structures that were
375 reactivated after each eruption. Around the central pie these structures are, to the SW, curved folds
376 whose wavelength of a few meters indicates a level of detachment located a few meters below the surface
377 (Fig. 12d). South of the mud pie the structures are a compressive bulge thrusted over the surrounding
378 vegetated plateau. As shown by the presence of an asymmetrical small lake at the thrust front, the
379 advancing bulge is flexuring the plateau (Fig. 12e), likely indicating the presence of a shallow pool of
380 plastic material making isostatic readjustment possible over short distances (Odonne et al., 2020). The
381 upper part of the thrusted block is deformed by opening cracks marking the extension of the folded outer
382 arc. Finally, the NE edge of the mud pie shows overlapping structures locally covered by the last
383 overflow of the mud pie (Fig. 12f). All these structures indicate a radial compression centered on the
384 emission point of the mudflows, which marks the spreading of the pie-like mudflow by pushing its
385 edges. On a larger scale, striae on active fault planes in the upper apron gullies all around the Akhtarma-

Pashaly MV, at least down to 50 m below the plateau, indicate that the plateau and steep upper apron together are spreading out radially (Fig. 15 in Odonne et al., 2020). The small reverse faults show lower dip values for thrusts than for back-thrusts (Table 1). The steep upper part of the apron is thus an active tectonic prism.

InSAR time series clearly indicates that no significant activity is noted from June 2017 to April 2018. In contrast, the period from April 2018 to April 2019 shows two contrasting patterns of activity: two interferograms (Figs. 13 a-2 and 13 a-4) show pervasive deformation over the whole plateau, with a complete loss of coherence during the interval that includes the April 27, 2018 eruption (Fig. 13 a-2). The end of July 2018 interval shows a complete loss of coherence over a 1-km diameter patch centered on the central mud pie and rather coherent fringes at the periphery of the plateau, indicating displacements limited to a few wavelengths of the interferometric signal (a few tens of cm). Other interferograms show coherent double or triple lobe patterns centered on the central pie (Fig. 13 a-3) or on the eastern pie (Fig. 13 a-1 and 13 a-6), indicating more localized deformation with lesser displacements.

We estimated the vertical and the easting components of displacement between July 24 and Sept. 4, 2018, using coherent ascending and descending track interferograms from Sentinel-1 (Fig. 13b). Over this interval, the easting displacement map exhibits a double-lobe pattern characteristic of horizontal expansion from the central mud pie. This extension is not accommodated by significant subsidence which is null or below InSAR accuracy. Sentinel-1 InSAR data clearly indicate that the surface deformation of the Akhtarma-Pashaly MV is marked by alternating periods of swelling and subsidence with overall spreading of the complete plateau.

The Bouguer anomaly map exhibits strong negative gravity anomalies up to -8 mGal with a wavelength of about 3 km (Fig 7b), values that clearly exceed those already recorded on mud volcanoes in Azerbaijan (Kadirov and Mukhtarov, 2004; Feyzullayev et al., 2005). An interesting feature is the spatial correlation between the shape of the plateau and the gravity anomaly pattern suggesting that the observed negative anomaly arises from a large flat-topped source located at shallow depth beneath the

plateau of the mud volcano. Inversion modeling of gravity data shows that a compact source with a mass deficit of -48×10^{10} kg located beneath the plateau at a depth of 50-100 m accounts quite well for the observed values, leading to rms of the residuals between the observed and the modeled data of 0.032 mGal (Figure 8b).

4. 4. Ayazakhtarma mud volcano

The Ayazakhtarma MV is a very flat mud volcano since its height above the surroundings does not exceed 35 m while the major axis of the flat plateau is almost 3 km long (Fig. 14 a) and relief variations over the plateau do not exceed 2 m. Field observations over 6 years show widespread deformation from one year to the next, in particular in the central area. Over a period of 6 years, the superimposition of georeferenced satellite images evidences an outward movement of the plateau centered on the main mud emission point, the maximum displacements (32 m, ca. 5 m/yr) being recorded in the SE sector (Fig. 14b). Vegetation is scarce on the surface of the mud volcano but completely absent from the central part where new pie-like mudflows have been appearing almost every year since we started our observations. We never observed any impact of a mud bomb on the surface of the Ayazakhtarma MV and the small mud pie whose emission we witnessed at the end of May 2016 was emplaced through quiet liquid flow, without projection of mud.

The surface of Ayazakhtarma deforms from a 250-300 m-radius central zone that is continuously expanding. The vegetated plateau around the center is dominantly affected by large strike slip fractures (Antonielli et al., 2014) over a radial distance of 300-400 m, beyond which the surface morphology is dominated by compressive structures interpreted as narrow circumferential pop-up blocks highlighted by twin lakes (Odonne et al., 2020). The most recent structures have formed in the NE sector of the mud volcano, where an indenter can be seen to move eastwards from one field campaign to the next. The frontal reverse fault surface of the indenter is marked by mud rubble collapse and is relayed by strike-slip lateral ramps (Fig. 14 c and d). Beyond the plateau edge, the entire apron of the Ayazakhtarma MV is a compressive wedge structured by numerous reverse faults whose striae indicate

438 a centrifugal movement (Fig. 8 in Odonne et al., 2020). As described on the Akhtarma-Pashaly MV,
439 dips of thrusts are lower than dips of back-thrusts (Table 1).

440 In contrast with the Akhtarma-Pashaly MV, Sentinel-1 InSAR interferograms indicate that the
441 activity of the Ayazakhtarma MV has been almost permanent over the two-year period of observation.
442 Short time interferograms (calculated over 12 days) generally show high coherence over the
443 Ayazakhtarma MV plateau, which indicates slow displacement, except in some instances where high
444 activity of the mud volcano led to a strong loss of coherence of the central part of the volcano (Fig15 a-
445 3). In that specific period, displacements are only resolved in the south and east quadrants, on the outer
446 500 m of each, indicating coherent displacements not exceeding about 6 cm and dying out at the edge
447 of the plateau in all cases.

448 The spatial pattern of ground displacement observed in coherent Sentinel-1 interferograms is
449 systematically centered on the central mud pie and remains consistent, with two lobes of opposite
450 polarity east and west of the center, the eastern lobe being about twice as large and with 2-3 times more
451 fringes that the western one. Several interferograms (Fig. 15.a-2 and Fig. 15.a-6 in particular) evidence
452 differential movement across the longest wrench faults observed at the surface of the Ayazakhtarma
453 MV.

454 We estimated the vertical and the easting components of displacement using coherent ascending
455 and descending track interferograms from Sentinel-1 during a period from 04 to 22 of October 2018
456 (Fig.15.b). Like on the Akhtarma-Pashaly MV, the easting displacement map exhibits a double-lobe
457 pattern characteristic of a horizontal expansion from the central mud pie, without detectable subsidence.
458 Such ground displacement field is in agreement with the centrifugal movement of the surface detected
459 by optical imaging satellite (Fig. 14 b) and with InSAR data from ALOS acquired between 2007-2011
460 presented in Iio and Furuya (2018).

461 The residual of the Bouguer anomaly map shows strong negative gravity anomalies up to -8
462 mGal with a wavelength of about 3 km (Fig. 7 b). The shape of the gravity anomaly strictly follows the
463 outline of the plateau. Inversion results shows that a large compact flat-topped source with a mass deficit

of -41×10^{10} kg located at shallow depth, a few tens of meters beneath the upper part of the mud volcano accounts very well for the gravity data, yielding 0.035 mGal of rms between the observed and the modeled data of Fig. 8 b.

5. Kinematic models of growth of conical and flat mud volcanoes

Field structural data give an insight into the local stress regime that prevailed during mud volcano formation. InSAR time series provide information on the periods of activity of mud volcanoes as well as on the resulting distribution of deformation at mud volcano scale, thereby constraining the areal distribution of low-viscosity subsurface mud bodies. Finally, gravimetric data provide information on the presence, and to some extent the distribution, of a low-density volume of mud near the surface of the mud volcano or at depth. The combination of the three data types makes it possible to propose an evolutive model of growth for the studied mud volcanoes.

5. 1. Kinematic model of the Otmanbozdag mud volcano

Older structures in Otmanbozdag MV are vegetated, while more recent ones are devoid of vegetation, exposing fresh gray mud breccia. The oldest part is therefore probably the peripheral ring that surrounds the mud volcano. Inside, inward-dipping reverse faults mark the outward spreading of the large mud pie that almost fills the crater floor (Fig. 4 a and Fig. 16 a). This stage corresponds to the small inflation of the mud pie, before the September 2018 eruption, observed by comparison of DEM and GNSS data (Fig. 5) and InSAR (Fig. 6.a). Then the succession of events that led to the eruption started in August 2018 with a deformation of the SE part of the crater (Fig. 6 a-2) and the beginning of deflation of the mud pie (Fig. 16b). The main eruption occurred on Sept 23, 2018 with release of hydrocarbons (Fig. 3b) and resulted in the breaching of the southern side of the peripheral rim and emission of 2-km-long mudflows down to the coastal plain; it also formed the extensional structures observed on the surface of the large pie (Fig. 4). These extensional structures reflect both the collapse of the pie and the extension caused by the overflow of the mud to the south (Fig. 16 c). Finally, the residual activity observed after

the eruption (Fig. 6 b) corresponds to final contraction by dehydration of both the mud pie and the outer mudflows. The distal termination of the flows underwent dehydration for a longer time than the slope part, likely due to higher thickness (compare the two panels in Fig. 6 b).

On the flanks of the crater breach, striae on fracture surfaces indicate a strike-slip movement compatible with the early time of the deformation of the pie during which a segment of the peripheral rim (Fig. 4 c) was pushed outwards before it gave way. The peripheral rim was then breached, the volume of mud initially stored above the breach level flowed out into gullies and the flanks of the mud volcano and the lateral margins of the outlet collapsed with an oblique downslope movement, indicating a combination of deflation and translation along the mudflow (Fig. 4 c).

Vegetation over the outer rim is an indication that this part has not been reactivated during the 2018 eruption. The low mass deficit observed from the gravity data (Fig. 7) also agrees with the occurrence of an eruption limited to the central upper part of the mud volcano.

A comparison between pre-eruption and post-eruption topographies indicates that a large volume of mud initially stored beneath the prismatic surface crust of the crater and above the altitude of the outlet to the south flowed out through the breach and down slope gullies to make the mudflow lobes in the coastal plain over a few hours. Evidence of gas release during the eruption (ballistic bomb impacts) and in the following hours (fig. 3 b) suggests that the pressure decrease corresponding with a 10-m deflation of the central dome caused exsolution of gas dissolved in the mud reservoir, and possibly triggered hydrocarbon release from deeper parts of the system.

It is therefore possible to propose a section of the structure of the Otmanbozdag MV (Fig. 16 d) showing the old caldera rim, the central pie which had progressively inflated into a dome before collapsing during the Sept. 2018 mud overflow as well as the extensional fractures formed over the entire summit of the mud volcano.

5. 2. Kinematic model of Toragay mud volcano

The structures that were active on the Toragay MV during this study are the rim fault of the collapse caldera, three pie-like mudflows on the caldera floor, and one radial mudflow. Each of the pre-2018 pie-like mudflows cover less than 20 % of the caldera floor and most are constrained by the edge of the caldera onto which they abut (Fig. 9 c and 17 b). Both larger pie-like mudflows emitted during the April 22, 2018 eruption extend beyond the caldera rim fault (Fig. 17 b). The eastern mudflow that initially flowed beyond the eastern rim collapsed along the rim fault later during the eruption, as evidenced by the striae affecting the fresh mud (Fig. 9 c-4 and 9c-5). On the western side, the pie-like mudflow compressed the edge of the caldera into a bulge (Fig. 9b and 9c-3) before bypassing it laterally on both sides and flowing westwards into the nearest gully heads. The gully-filling mudflow extends 500 m beyond the crater rim and is 8-10 m wide on average. The high length/width ratio of the flow seems to indicate a very fluid mud (Fig. 9 b).

InSAR time series (Fig. 10) seem to agree with a discontinuous operation over time of small pies that can sometimes overflow from the summit into slope gullies of the mud volcano, resulting in a loss of coherence in InSAR signals. Gravimetric modeling (Fig. 8) shows a ~ 300 m-diameter mass deficit centered on the mud volcano crater.

The model we propose for the subsurface structure of the Toragay MV (Fig. 17 c) is based on visual evidence of subsidence of the 400-m diameter caldera floor during the April 22, 2018 eruption combined with the gravimetry model: the outline of the low-density body roughly coincides with the surface expression of the caldera rim faults. Its negative relief with respect to the outer rim constrains the effusion of intra-crater pie-like flows, and the caldera border fault locally affects the edge of pies formed during the same eruption, while it is sealed in some places by deposits of the same eruption. This indicates that fault activity took place during the eruption and records transfer of material from the mud reservoir up to the surface, caldera floor subsidence compensating for loss of material in subsurface. Local variations of timing reflect the fact that mud is emitted through two localized outlets while fault activity reflects the downbuilding of the whole reservoir at depth. Gravity measurements indicate a possible mud chamber at a shallow depth of about 200 m. The existence of two separate mud and flame

emission points on April 22, 2018, indicates the presence of several conduits leading from the subsurface chamber to the caldera floor that were active at the same time. The fact that the western conduit at least is different from all previous ones (1988 or older) suggests that conduits are short-lived features, i.e. heal over a few decades.

5. 3. Kinematic model of the Akhtarma-Pashaly and Ayazakhtarma mud volcanoes

Both flat mud volcanoes studied here have a tectonically active surface and an expanding border. The Akhtarma-Pashaly MV underwent activity on three of its plateau mud pies over the last 6 years, with emission of mud and indications of some mud bomb impacts. In contrast, none of the Ayazakhtarma mudflows we could observe during this study showed evidence of mud bomb impacts and the mud seems to be emitted only from the central area which is constantly changing (Figs. 14 and 15). In both mud volcanoes the plateau is almost flat with altitude variations between center and periphery not exceeding two meters. The plateau surface is marked by large strike-slip structures that terminate at the edge of the plateau, which is growing up and expanding out as shown by the geometric pattern of active faults in the apron. A tectonic prism is currently forming around each of these mud volcanoes, characterized by conjugate thrusts (dipping towards the mud volcano) and back thrusts, the latter set with higher dips (Table1). Neither of the flat mud volcanoes has a raised peripheral rim that could indicate a collapse caldera.

Sentinel-1 InSAR time series (Figs. 13 and 15) show in both cases that surface activity alternates between phases of widely distributed displacements and phases where deformation is slow and restricted to the surroundings of the mud emission points. It should be noted that the activity of individual pie like mudflows on the Akhtarma-Pashaly MV is episodic, with recurrence times between eruptions ranging from 1 year to several decades, as evidenced by satellite pictures. Gravimetry data indicate under each mud volcano a significant mass deficit, up to -8 mGal of variation along 1 km (Fig. 7b), which is attributed to a mass of mud rich in water and therefore also more fluid. In both cases, the

566 modeled subsurface low-density body is concentric with the mud volcano at a relatively shallow depth
567 (Fig. 8b).

568 The kinematic model proposed for flat mud volcanoes (Fig. 18) is based on two key
569 characteristics: first their very flat character, with altitude variations of the plateau within the same range
570 as those observed on the Otmanbozdag MV caldera after the 2018 eruption (ca. 1 m), in spite of repeated
571 mud emission in the central part (Ayazakhtarma MV) or at discrete emission points (Akhtarma-Pashaly
572 MV) that pile up without leading to increased elevation; second, the tectonic deformation of the plateau
573 dominated by strike-slip faults, accommodating large displacements with very limited vertical
574 movement. Both characteristics require the presence of a shallow plastic body that can rapidly
575 accommodate deformation over large areas. The lateral extent of the plastic body is delineated using the
576 area affected by strike-slip faults. It extends all the way out to the plateau edge, which is thus the outer
577 limit of the underlying shallow plastic body. As regards its thickness, the mass deficit modeled from
578 variations of the gravity field within the limits of realistic density variations impose an order of
579 magnitude of several hundred meters. Beyond the plateau edge, the apron grows as a tectonic prism with
580 a slope between 6 and 10 ° (Fig. 18 d), which indicates a basal friction greater than that of liquid mud.
581 Dahlen (1984) has shown that the shape of such prisms is characterized by their surface slope (α) and
582 basal slope (β), which in turn depend on the internal friction angle of the material (φ) as well as the angle
583 of friction at the base of the prism (φ_b). The internal friction angle of the material can be estimated from
584 Mohr circle by the angle between the conjugate faults (Ramsay, 1967). The average values calculated
585 for Ayazakhtarma are 43° and 58° for thrusts and backthrusts, respectively, while they are 31° and 47°
586 for Akhtarma-Pashaly. The combined set of values gives averages of 40° and 54° for thrusts and
587 backthrusts, which we consider more representative given the small number of possible measurements
588 (Table 1). This results in an angle between the two families of faults of 94°, meaning that the internal
589 friction angle of the material must be very low, close to 0°. The angle between σ_1 and the basal sliding
590 surface is deduced from the tilting of the faults in the prism (Dahlen, 1984), here it is estimated at 7°
591 (Fig. 18 d). All this indicates a high basal friction (φ_b) in prisms whose surface slopes are quite high, 6°

592 for the Ayazakhtarma MV and 10° for the Akhtarma-Pashaly MV, and a very low value of β (2° or 0°),
593 which agrees with the expansion of the edge of the Ayazakhtarma onto a very slightly inclined plain.
594 As a result, flat mud volcanoes grow by pushing their border prism outwards. Due to the large
595 mass of mud close to the surface, it is difficult to determine whether one or more pipes feed the mud
596 volcanoes: the emission points of the different mud pies (Fig. 18 a and b) may correspond either to
597 multiple feeders below the shallow chamber or to episodic local weakness zones of the thin surface crust
598 above the chamber, that would heal after a few eruptions and be replaced by another.
599
600 **6. Discussion**
601 6. 1. Evidence for mud chambers
602 In magmatic volcanic systems, the existence of chambers has been revealed from a combination of
603 geophysical measurements (review in Iyer, 1984), including gravity field measurements (Furuya et al.,
604 2003), and caldera subsidence that has been related to magma withdrawal from a deep magma body
605 since the late 19th Century (Cole et al., 2005 and see refs. in Galland et al., 2015). On mud volcanoes,
606 subsidence-caldera-like features are common and have been understood as "forming from the evacuation
607 of material from the subsurface" (Bonini and Mazzarini, 2010), and Deville et al. (2006) state that
608 collapse structures and calderas suggest the occurrence of liquid mud chambers at depth. However, the
609 interpretation of a funnel-shaped caldera is proposed by Mauri et al. (2018) on the LUSI mud volcano,
610 where modeling of density changes seems to rule out the existence of a preexisting deep chamber. There
611 is thus an uncertainty remaining as whether caldera formation requires the presence of a large preexisting
612 mud chamber or can form progressively as mud is formed in the subsurface and evacuated (the
613 "depletion zone" concept of Kirkham et al. (2017). Our gravity models show that the studied mud
614 volcanoes are underlain by low-density bodies whose thickness is in the 100-500 m range, 1-2 orders of
615 magnitude higher than the amount of collapse associated with individual eruptions or the estimated
616 thickness of individual mudflows. These data therefore evidence the presence of real mud chambers

617 below the studied mud volcanoes, i.e. permanent volumes of low-density material a small fraction of
618 which is released at each eruption.
619
620 6. 2. Summit caldera: evidence for a deep chamber
621 The Toragay MV shows a clear rim fault along which piston-like collapse occurred during the 2018
622 eruptions, signing collapse of a summit caldera. The pre-collapse morphology, as we observed it before
623 2018, did show a peripheral rim with a steep inward slope, but no evidence for a fault scarp. Previous
624 eruptions of the Toragay MV date back to the mid 1980's (Aliev et al., 2015). It thus appears that
625 weathering over a few tens of years obliterates rim fault scarps only leaving an inward slope at the angle
626 of repose of dry mud. The peripheral rim of the Otmanbozdag MV shows precisely this type of
627 morphology, which we interpret to indicate that it is the weathered remnant of caldera subsidence
628 associated with an eruption pre-dating the first satellite pictures available to us (2009 on Google Earth).
629 Considering that the rim is much higher than that of the Toragay MV and its diameter about twice larger,
630 the volume emitted during that old eruption must have been quite large. Historical records dating back
631 to 1810 (Aliev et al., 2015, Aliyev et al., 2019) mention an eruption on Nov. 23, 1904, where a mudflow
632 4 times larger than the 2018 one was emitted (Golubiatnikov, 1904; cited in Aliev et al., 2015). The
633 crater rim may have formed at that time or earlier. In contrast, the elements of low-relief peripheral rim
634 observed around the Ayazakhtarma MV are clearly compressional, and neither of the flat mud volcanoes
635 show indications of caldera-type subsidence. Calderas thus appear as a specific feature of conical mud
636 volcanoes.
637 The calderas of magmatic volcanoes are due to withdrawal of material from the magma
638 chamber at depth, which leads to the formation of circular fractures and collapse of the summit of the
639 volcano (Komuro, 1987; Scandone, 1990; Branney, 1995; Cole et al., 2005). The development of such
640 concentric structures has been studied using analog models (Marti et al., 1994; Troll et al., 2002;
641 Holohan et al., 2005; Acocella, 2007; Acocella, 2021). Recent research on the subject includes
642 examination of the effect of magma reinjection following a deflation of the magma chamber (Bonini et

al., 2021) or the interaction between chamber activity and the presence of preexisting faults in the overburden (Maestrelli et al., 2021). Analogue and numerical modeling have evidenced that the geometry of surface collapse following emptying of an underground volume depends on the thickness of the removed volume and on the aspect ratio of the roof. In order to generate a fault-bounded surface collapse, the volume-to-be-removed must first be thick enough to ensure that material removal at depth is not absorbed by intra-roof deformation/dilatancy. The thickness/width ratio of the roof, noted R, has then been shown from analogue modeling to influence the style of surface subsidence: for $R<0.7$, the collapsed roof is surrounded by normal faults, while for $R>0.7$ it is limited by subvertical reverse faults (Roche et al., 2000; Galland et al., 2015; Marti et al., 1994). The presence of summit calderas on both conical mud volcanoes is therefore indicative of the presence of mud chambers below at a depth of at least 0.7 times the caldera diameter, i.e. ca. 300 m on the Toragay MV and ca. 500 m on the Otmanbozdag MV. We have no structural evidence for the presence of deep chambers below flat mud volcanoes.

6. 3. Evidence for shallow mud chambers

Leaving aside mass deficit, the main other line of evidence for the presence of fluid mud beneath mud volcanoes is the presence of flat surfaces that indicate isostatic equilibrium above a low-strength sediment body. This process was discussed by Odonne et al. (2020) to account for the flatness of the plateau of the Ayazakhtarma MV, as well as for the morphology of twin lakes indicating pop-up blocks, and also applies to the Akhtarma-Pashaly MV. The height of the critical tectonic prism surrounding the plateau gives a maximum limit on the thickness of the roof, as discussed in section 5.3. However, it does not provide any indication on the thickness of the low-strength mud body.

The deflation to horizontal of the floor of the caldera of the Otmanbozdag MV after the 2018 eruption, as observed visually and measured from GNSS (Fig. 5) is similarly well explained by the presence of a body of soft mud just below the originally convex-up surface, i.e. a very shallow mud chamber. The eruption of the Otmanbozdag MV was accompanied by the formation of normal faults

and tilted blocks on the edges gradually replaced by tension fractures organized in diamonds (Fig. 4 b). This type of structure develops at the top of magmatic volcanoes during the collapse of the surface (Branney, 1995) and in analog models in case of a thin cover (Roche et al., 2000). The soft mud body would have filled progressively by mud migrating up from deeper levels, progressively building the convex-up structure akin to lava domes (cf. Galland et al., 2015). The breaching of the crater rim on Sept. 23, 2018 let all the mud stored higher than the outlet sill flow out downslope, forming the 2 km-long mudflow. The corresponding mud chamber must therefore lie very shallow, a few meters only beneath the mud volcano surface. We have no direct information on the depth of this shallow chamber, but the flat character of the caldera floor after the 2018 eruption indicates that there must be a soft mud body remaining after the eruption. The OBMV thus has two separate chambers, a shallow one evidenced by the flattening of the pre-eruption dome during the Sept. 2018 eruption and a deep one (deeper than 0.7 times the crater diameter, i.e., ca. 500 m) from the presence of the collapse caldera and gravimetry modeling. Moreover, the volume of low-deficit material and the average depth from modeling derived from post-eruption data indicate that the lower chamber is still present after eruption and is the larger.

6.4 Compared modes of growth of flat vs. conical mud volcanoes

Mud emission to the surface on both conical and flat mud volcanoes dominantly occurs by emission of pie-like mudflows. We could not see any systematic difference between flow morphology or mud rheology between the two mud volcano types, with the exception of the rare and violent eruptions with large gas flames and projection of mud bombs described in Aliev et al. (2015), which are strictly limited to conical volcanoes. Such a violent feeding mode allows vertical growth of conical mud volcanoes. Moreover, collapse calderas and associated circular rim faults appear characteristic of conical mud volcanoes while flat mud volcanoes have a compressive outer margin, without a caldera in the two examples we studied. Deformation at the scale of the full edifice is thus sharply contrasted between the two types of edifices: flat mud volcanoes grow by continuous radial expansion of the whole edifice, the peripheral rim being an actively growing critical Coulomb wedge; in contrast, radial deformation in

conical MVs is buttressed by the fixed crater rim. When mud supply to the surface of conical mud volcanoes exceeds what can be accommodated in the crater, excess mud is released by rim breaching and overflow towards the flanks. One way of describing this contrast is to oppose two styles of rim deformation: episodic, by localized failure and breaching on conical mud volcanoes and continuous by distributed compression and radial expansion all around flat mud volcanoes.

Our observations on a small number of mud volcanoes and a relatively short time span suggest that eruption recurrence times are shorter for flat than for conical mud volcanoes, leaving less time for mud desiccation at the surface and flow strengthening in subsurface by compaction in the former case. This could be a consequence of the result from two factors: 1) the depth of the mud chamber, a few meters below surface for the former set and several hundred meters for the latter; and 2) the fact that conical mud volcanoes with calderas have their expansion buttressed laterally, requiring more energy to breach the chamber roof than in flat mud volcanoes without calderas, whose growth is dominated by radial expansion facilitating breaching of the roof. The difference in recurrence time in turn is likely to favor the preservation of soft mud close to the surface of flat mud volcanoes, leading to permanent isostatic readjustment of intra-plateau deformations. The longer recurrence time of eruptions on conical mud volcanoes means that they grow both by the mud stacking following the violent eruptions and by the progressive hardening of the mudflows and possibly of the mud remaining in the mud chambers.

7. Conclusions

Our field studies over the period from 2014 to 2019 and InSAR time series show highlight differences in type of activity between mud volcanoes belonging to two end-members of the spectrum of mud volcano morphologies, the conical and flat types.. Flat mud volcanoes are regularly fed and are constantly deforming while conical mud volcanoes are fed discontinuously, alternating between active periods and moments of rest.

Flat mud volcanoes show inflows of surface mud which spread out to form thin pie-like mudflows. The stacking of these mudflows does not increase the elevation of the surface since the whole

721 rests on a thick layer of fluid mud. Then, the volume increase of flat volcanoes that are constantly fed
722 by fresh mud is accommodated by an increase in surface area obtained by pushing the borders outwards,
723 forming a tectonic prism at their periphery. InSAR data show this horizontal spreading during eruptions.
724 The presence of a large volume of mud is attested by the large mass deficit (residual gravity signal up
725 to -8 mGal), which does not extend beyond the mud volcano and which is located close to the surface.
726 We did not observe subsidence related to material removal from this mud chamber and no caldera-like
727 structure has been observed on flat mud volcanoes that could indicate such a historical drain.

728 In contrast, conical mud volcanoes have episodic but more violent eruptions, with projection
729 of bombs and gas flames. They show a smaller mass deficit at their center and calderas are always
730 present at the top. Due to buttressing by caldera rim, conical mud volcanoes generally accommodate
731 mud influx by intra-caldera doming and/or mudpie stacking, interrupted by occasional episodes of
732 breaching that sheds excess mud volume out into one of the slope gullies. At the Otmanbozdagh MV,
733 what remained in the crater of the mud volcano after the latest major eruption is the dried surface crust
734 of a shallow mud body, some of which was evacuated laterally during the eruption. The remnants of the
735 crust lie almost flat and were completely deformed during the collapse. On the Toragay MV, the caldera
736 subsided along the rim fault during eruptions. It constrained the effusion of smaller pie-like mudflows
737 and cut the edge of larger ones that flowed across the rim fault in the initial stages of eruption, before
738 subsidence started.

739 One key finding from this study is that both flat and conical mud volcanoes may have mud
740 chambers in their subsurface feeder systems. The chambers we identify are concentric with the surface
741 mud volcano and their outline in map view approximates that of the summit caldera of conical mud
742 volcanoes and of the plateau of flat mud volcanoes. Mud chambers are 100-500 m thick, much larger
743 and apparently thicker below flat MVs than below conical MVs. Only one of the two studied conical
744 MVs showed evidence for two stacked mud chambers, one within a few meters of the surface and the
745 other several hundred meters deep. It was not possible from our current dataset to determine whether
746 the other three MVs had one or several stacked mud chambers.

ACKNOWLEDGMENTS

We would like to thank TOTAL who supported this research. We are also grateful to the Institute of Geology and Geophysics of Azerbaijan, National Academy of Sciences for substantial help during field work. We wish to express our warmest thanks to Rassim Akhundov and all the staff of Total E&P Absheron B.V. who kindly provided technical assistance during field missions. We thank CNRS INSU and RESIF-Gmob who graciously lent us a gravimeter for the 2018 and 2019 field work. PALSAR data from the ALOS satellite mission operated by the Japanese Aerospace Exploration Agency (JAXA) were used under the terms and conditions of the fourth ALOS 2 Research Announcement (project 3101). We thank the European Space Agency for providing us with the SENTINEL-1 data and the CNES for facilitating the gravity, InSAR and GNSS data analysis in the GET Research Laboratory. We would like to thank Stéphane Bonnet who produced the first mosaics for our drone pictures.

References

Acocella, V. (2007). Understanding caldera structure and development: An overview of analogue models compared to natural calderas. Earth-Science Reviews, 85(3-4), 125-160. doi:10.1016/j.earscirev.2007.08.004.

Acocella, V. (2021). Calderas. In Volcano-Tectonic Processes (pp. 163-203). Springer, Cham.

Aliev, Ad. A., Guliev, I.S., Dadashov, F. H., Rahmanov, R.R., 2015. Atlas of the world Mud Volcanoes. Nafta Press Publishing House, 321 p.

Aliyev, Ad. A., Guliyev I. S., Rahmanov, R. R., 2019. Catalogue of recorded of mud volcano eruptions of Azerbaijan (2008-2018). Institute of Geology and Geophysics of Azerbaijan, National Academy of Sciences. 65 p.

Alizadeh, A. A., 2008. Geological map of Azerbaijan Republic, Scale 1: 500,000, with Explanatory Notes. *Baki Kartoqrafiya Fabriki*

773 Antonielli, B., Monserrat, O., Bonini, M., Righini, G., Sani, F., Luzi, G., Feyzullayev A. A., Aliyev, C. S., 2014.
774 Pre-eruptive ground deformation of Azerbaijan mud volcanoes detected through satellite radar
775 interferometry (DInSAR): Tectonophysics, 637, 163-177. http://dx.doi.org/10.1016/j.tecto.2014.10.005
776 Blouin, A., Imbert, P., Sultan, N., & Callot, J. P. (2019). Evolution model for the Absheron mud volcano: From in
777 situ observations to numerical modeling. Journal of Geophysical Research: Earth Surface, 124(3), 766-794.
778 Blouin, A., Sultan, N., Pierron, A., Imbert, P., & Callot, J.-P., 2020. Evolution model for the Absheron mud
779 volcano: from stratified sediments to fluid mud generation. *Journal of Geophysical Research: Earth*
780 *Surface*, *125*, e2020JF005623. https://doi. org/10.1029/2020JF005623
781 Bonini, M., 2012. Mud volcanoes: Indicators of stress orientation and tectonic controls. Earth-Science Reviews,
782 115, 121-152.
783 Bonini M., Rudolph M. L., Manga M., 2016. Long and short-term triggering and modulation of mud volcano
784 eruptions by earthquakes. Tectonophysics, 672-673, 190-211.
785 http://dx.doi.org/10.1016/j.tecto.2016.01.037
786 Bonini, M., Mazzarini, F., 2010. Mud volcanoes as potential indicators of regional stress and pressurized layer
787 depts. Tectonophysics, 494, 32-47. https://doi:10.1016/j.tecto.2010.08.006
788 Bonini, M., Maestrelli, D., Corti, G., Del Ventisette, C., Moratti, G., Carrasco- Núñez, G., ... & Montanari, D.
789 (2021). Modeling Intra- Caldera Resurgence Settings: Laboratory Experiments With Application to the
790 Los Humeros Volcanic Complex (Mexico). Journal of Geophysical Research: Solid Earth, 126(3),
791 e2020JB020438. https://doi.org/10.1029/2020JB020438
792 Branney, J. M., 1995. Downsag and extension at calderas. New perspectives on collapse geometries from ice-melt,
793 mining, and volcanic subsidence. Bull. Volcanol., 57, 303-318.
794 Brunet, M.-F., Korotaev, M. V., Ershov, A. V., Nikishin, A. M., 2003. The South Caspian Basin: a review of its
795 evolution from subsidence modelling. Sedimentary Geology, 156, 119-148.
796 Chen, C.W., Zebker, H.A., 2002. Phase unwrapping for large SAR interferograms: Statistical segmentation and
797 generalized network models. IEEE Transactions on Geoscience and Remote Sensing 40, 1709–1719.
798 Cita, M. B., Ryan, W. F. B., Paggi, L., 1981. Prometheus mudbreccia: An example of shale diapirism in the
799 Western Mediterranean Ridge, *Ann. Geol. Pays Hell.*, *30*, 543–570.
800 Cole J. W., Milner D. M., Spinks K. D., 2005. Calderas and caldera structures: a review. Earth-Science Reviews,
801 69, 1-26. doi:10.1016/j.earscirev.2004.06.004

Dahlen, F. A., 1984. Noncohesive critical coulomb wedges: an exact solution: Journal of Geophysical Research, 89, 10125-10133.

Davies, R. J., Stewart S. A., 2005. Emplacement of giant mud volcanoes in the South Caspian Basin: 3D seismic reflection imaging of their root zones. Journal of the Geological Society, London, 162, 1-4.

Dercourt, J., Zonenshain, L., Ricou, L., Kazmin, V., Le Pichon, X., Knipper, A., Grandjacquet, C., Sbortshikov, I., Geyssant, J., Lepvrier, C., Pechersky, D., Boulin, J., Sibuet, J., Savostin, L., Sorokhtin, O., Westphal, M., Bazhenov, M., Lauer, J., Biju-Duval, B., 1986. Geologic evolution of the Tethys belt from the Atlantic to the Pamirs since the Lias, *in* Aubouin, L., Le Pichon, X., and Monin, A., eds., Evolution of the Tethys: Tectonophysics, 123, nos. 1–4, 241–315.

Deville, E., Battani, A., Griboulard, R., Guerlais, S., Herbin, J. P., Houzay, J. P., Muller, C., Prinzhofer, A., 2003. The origin and processes of mud volcanism: new insights from Trinidad. In: Subsurface Sediment Mobilization, P. Van Rensbergen, R. R. Hillis, A. J. Maltman & C. K. Morley (eds). Geological Society Spec. Pub. 216, 475-490.

Deville, E., Guerlais, S.-H., Callec, Y., Griboulard, R., Huyghe, P., Lallemant, S., Mascle, A., Noble, M., Schmitz, J., and the collaboration of the Caramba working group, 2006, Liquefied vs stratified sediment mobilization processes: Insight from the South of the Barbados accretionary prism. Tectonophysics 428, 33–47. doi:10.1016/j.tecto.2006.08.011

Devlin, W. J., Cogswell, J. M., Gaskins, G. M., Isaksen, G. H., Pitcher, D. M., Puls, D. P., Stanley, K. O., Wall, G. R. T., 1999. South Caspian Basin: Young, cool, and full of promise. GSA Today, 9, 1-9.

Dimitrov, L. I., 2002. Mud volcanoes - the most important pathway for degassing deeply buried sediments: Earth-Science Reviews, 59(1), 49-76.

Dupré, S., Buffet, G., Mascle, J., Foucher, J. P., Gauger, S., Boetius, A., Marfia, C., the AsterX AUV Team, Quest ROV Team & BIONIL Scientific Party, 2008. High-resolution mapping of large gas emitting mud volcanoes on the Egyptian continental margin (Nile Deep Sea Fan) by AUV surveys: Marine Geophysical Researches, 29(4), 275-290. https://doi: 10.1007/s11001-009-9063-3

Dupuis, M., Imbert, P., Vendeville, B. C., Odonne, F., 2019. Mud volcanism by repeated roof collapse: 3D architecture and evolution of a mud volcano cluster offshore Nigeria. Marine and Petroleum Geology, 110, 368-387. https://doi.org/10.1016/j.marpetgeo.2019.07.033

Feseker, T., Pape T., Wallmann K., Klapp S. A., Schmidt-Schierhorn F., Bohrmann G., 2009. The thermal structure of the Dvurechenskii mud volcano and its implications for gas hydrate stability and eruption dynamics. Marine and Petroleum Geology, 26, 1812-1823.

Feyzullayev, A. A., Kadirov, F. A., Aliyev, C. S., 2005. Mud volcano model resulting from geophysical and geochemical research. In: Mud Volcanoes, Geodynamics and Seismicity, G. Martinelli and B. Panahi (eds), Springer, Netherlands, 251-262.

Forte, A. M., Cowgill, E., Bernardin, T., Kreylos, O., Hamann, B., 2010. Late Cenozoic deformation of the Kura fold-thrust belt, southern Greater Caucasus. G. S. A. Bull., 122, 465-486. doi: 10.1130/B26464.1

Fournier, D., Davis, K., Oldenburg, D.W., 2016. Robust and exible mixed- norm inversion. SEG Annual Meeting 1542{1547URL: http://library.seg.org/doi/10.1190/segam2016-13821093.1.

Fowler, S. R., Mildenhall, J., Zalova, S., Rileyn G., Elsley, G., Desplanques, A., Guliyev, F., 2000. Mud volcanoes and structural development on Shah Deniz. Journal of Petroleum Science and Engineering, 28, 189-206.

Furuya, M., Okubo S., Sun W., Tanaka Y., Oikawa J., Watanabe H., 2003. Spatitemporal gravity changes at Miyakejima Volcano, Japan: Caldera collapse, explosive eruptions and magma movement. Journal of Geophysical Research, 108, B4, 2219. Doi:10.1029/2002JB0011989,2003.

Gabalda, G., Bonvalot, S., Hipkin, R., 2003. CG3TOOL: an interactive computer program to process Scintrex CG-3/3M gravity data for high-resolution applications. Computers & Geosciences, 29, 155–171.

Galland, O., Holohan E., van Wyk de Vries B., Burchardt S.et al., 2015. Laboratory modelling of volcano plumbing systems: a review. Advances in Volcanology, DOI: 10.1007/11157_2015_9

Guliev, I. S., Feizullayev A. A., 1996. Geochemistry of hydrocarbon seepages in Azerbaijan. In: Hydrocarbon migration and its near-surface expression. D. Schumacher and M. A. Abrams (eds). AAPG Memoir 66, 63-70.

Henry, P.-H., Le Pichon, X., Lallemant, S., Foucher, J.-P., Westbrook, G., Hobart, M., 1990. Mud volcano field seaward of the Barbados accretionary complex: A deep-towed side scan sonar survey. Journal of Geophysical Research, 95, B6, 8917-8929.

Higgins, G. E., Saunders, J. B., 1974. Mud Volcanoes – their Nature and Orogin. Verhand. Naturf. Ges. Basel, 84, 1, 101-152.

857 Holohan, E. P., Troll, V. R., Walter, T. R., Münn, S., McDonnell, S., & Shipton, Z. K. (2005). Elliptical calderas
858 in active tectonic settings: an experimental approach. Journal of Volcanology and Geothermal Research,
859 144(1-4), 119-136. https://doi.org/10.1016/j.jvolgeores.2004.11.020
860 Hovland, M., Hill, A., Stokes, D., 1997. The structure and geomorphology of the Dashgil mud volcano, Azerbaijan.
861 Geomorphology, 21(1), 1-15.
862 Iio, K., Furuya, M., 2018. Surface deformation and source modeling of Ayaz-Akhtarma mud volcano, Azerbaijan
863 as detected by ALOS/ALOS-2 In SAR. Earth and Planetary Science, 5:61, 1-16.
864 https://doi.org/10.1186/s40645-018-0220-7
865 Iyer, H. M. (1984). Geophysical evidence for the locations, shapes and sizes, and internal structures of magma
866 chambers beneath regions of Quaternary volcanism. Philosophical Transactions of the Royal Society of
867 London. Series A, Mathematical and Physical Sciences, 310(1514), 473-510.
868 Inan, S., Yalcin, M. N., Guliev, I. S., Kuliev, K. and Feizullayev, A. A., 1997. Deep petroleum occurences in the
869 lower Kura depression, south Caspian Basin, Azerbaijan: An organic geochemical and basin modelling
870 study: Marine and Petroleum Geology, 14, 731-762.
871 Jakubov, A.A., Ali-Zade, A.A., Zeinalov, M.M., 1971. Mud Volcanoes of the Azerbaijan SSR: Atlas. Elm-
872 Azerbaijan Acad. Of Sci. Pub. House, Baku.
873 Javanshir, R. J., Riley, G. W., Duppenbecker, S. J., & Abdullayev, N. (2015). Validation of lateral fluid flow in an
874 overpressured sand-shale sequence during development of Azeri-Chirag-Gunashli oil field and Shah Deniz
875 gas field: South Caspian Basin, Azerbaijan. Marine and Petroleum Geology, 59, 593-610.
876 Kadirov, F. A., Mukhtarov, A. Sh., 2004. Geophysical fields, deep structure, and dynamics of the Lokbatan mud
877 volcano. Izvestiya, Physics of the Solid Earth, 40(4), 327-333.
878 Kadirov, F., Floyd, M., Alizadeh, A., Guliev, I., Reilinger, R., Kuleli, S., King, R., Toksoz, M. N., 2012.
879 Kinematics of the eastern Caucasus near Baku, Azerbaijan. Nat Hazards, 63, 997-1006. https://doi:
880 10.1007/s11069-012-0199-0
881 Kadirov, F. A., Guliyev, I. S., Feyzullayev, A. A., Safarov, R. T., Mammadov, S. K., Babayev, G. R., Rashidov,
882 T. M., 2014. GPS-Based crustal deformations in Azerbaijan and their influence on seismicity and mud
883 volcanism. Izvestiya, Physics of the Solid Earth, 50, 814-823. https://doi: 10.1134/S1069351314060020

884 Karyono, K., Obermann, A., Lupi, M., Masturyono, M., Hadi, S., Syafri, I., Abdurrokhim, A., Mazzini, A., 2017.
885 Lusi, a clastic-dominated geysering system in Indonesia recently explored by surface and subsurface
886 observations. Terra Nova, 29,13-19. doi:10.1111/ter.12239
887 Kirkham, C., Cartwright, J., Hermanrud, C., Jebsen, C., 2017. The spatial, temporal and volumetric analysis of a
888 large mud volcano province within the Eastern Mediterranean. Marine and Petroleum Geology, 81, 1-16.
889 Komuro, H., 1987. Experiments on cauldron formation: A polygonal cauldron and ring fractures. Journal of
890 Volcanology and Geothermal Research, 31, 139-149.
891 Kopf, A. J., 2002. Significance of mud volcanism. Reviews of Geophysics, 40, 1-52.
892 https://doi:10.1029/2000RG000093
893 Kopf, A., & Behrmann, J. H. (2000). Extrusion dynamics of mud volcanoes on the Mediterranean Ridge
894 accretionary complex. Geological Society, London, Special Publications, 174(1), 169-204.
895 Lance, S., Henry, P., Le Pichon, X., Lallemant, S., Chamley, H., Rostek, F., Faugères J.-C., Gonthier E., Olu, K.,
896 1998. Submersible study of mud volcanoes seaward of the Barbados accretionary wedge: sedimentology,
897 structure and rheology: Marine Geology, 145(3-4), 255-292.
898 Le Pichon, X., Foucher, J. P., Boulègue, J., Henry, P., Lallemant, S., Benedetti, M., Avedik F., Mariotti, A., 1990.
899 Mud volcano field seaward of the Barbados accretionary complex: a submersible survey: Journal of
900 Geophysical Research: Solid Earth, 95(B6), 8931-8943.
901 Loncke, L., Mascle, J., Fanil Scientific Parties, 2004. Mud volcanoes, gas chimneys, pockmarks and mounds in
902 the Nile deep-sea fan (Eastern Mediterranean): geophysical evidences. Marine and Petroleum Geology, 21,
903 669–689. doi:10.1016/j.marpetgeo.2004.02.004
904 Maestrelli, D., Bonini, M., Delle Donne, D., Manga, M., Piccardi, L., Sani, F., 2017. Dynamic triggering of mud
905 volcano eruptions during the 2016-2017 Central Italy seismic sequence. Journal of Geophysical Research:
906 Solid Earth. 122, 9149-9165. http://doi.org/10.1002/2017JBO14777.
907 Maestrelli, D., Bonini, M., Corti, G., Del Ventisette, C., Moratti, G., & Montanari, D. (2021). Exploring fault
908 propagation and the role of inherited structures during caldera collapse through laboratory experiments.
909 Journal of Volcanology and Geothermal Research, 414, 107232.
910 https://doi.org/10.1016/j.jvolgeores.2021.107232

911 Maestro, A., Bohoyo, F., Corral, R., 2019. Recent deformation state from morphological analysis of mud volcanoes
912 in the Gulf of Cadiz (southwestern part of the Iberian Atlantic Margin). Journal of Geodynamics, 132,
913 101653. doi.org/10.1016/j.jog.2019.101653.
914 Manga, M., Brumm, M., Rudolph, M. L., 2009. Earthquake triggering of mud volcanoes. Marine and Petroleum
915 Geology, 26, 1785-1798. doi:10.1016/j.marpetgeo.2009.01.019.
916 Marti, J., Ablay, G. J., Redshaw, L. T., Sparks, R. S. J., 1994. Experimental studies of collapse calderas. Journal
917 of the Geological Society, London, 151, 919-929.
918 Marty, J.C., Loyer, S., Perosanz, F., Mercier, F., Bracher, G., Legresy, B., Portier, L., Capdeville, H., Fund, F.,
919 Lemoine, J.M., Biancale, R., 2011. GINS: the CNES/GRGS GNSS scientific software, 3rd international
920 colloquium scientific and fundamental aspects of the galileo programme. In: ESA Proceedings WPP326,
921 31 August – 2 September 2011, Copenhagen, Denmark.
922 Massonnet, D., Feigl, K.L., 1998. Radar interferometry and its application to changes in the Earth's surface. Rev.
923 Geophys 36, 441–500.
924 Mauri, G., Husein, A., Mazzini, A., Irawan, D., Sohrabi, R., Hadi, S., Prasetyo, H., Miller, S. A., 2018. Insights
925 on the structure of Lusi mud edifice from land gravity data. Marine and Petroleum Geology, 90, 104-115.
926 doi.org/10.1016/j.marpetgeo.2017.05.041.
927 Mazzini, A., Svensen, H., Akhmanov, G. G., Aloidi, G., Planke, S., Malthe-Sørensen, A., Istadi, B., 2007.
928 Triggering and dynamic evolution of the LUSI mud volcano, Indonesia. Earth and Planetary Science
929 Letters, 261, 375-388. doi:10.1016/j.epsl.2007.07.001
930 Mazzini, A., Ivanov, M. K., Nermoen, A., Bahr, A., Bohrmann, G., Svensen, H., Planke, S., 2008. Complex
931 plumbing systems in the near subsurface: Geometries of authigenic carbonates from Dolgovskoy Mound
932 (Black Sea) constrained by analogue experiments. Marine and Petroleum Geology, 25, 457-472.
933 doi:10.1016/j.marpetgeo.2007.10.002
934 Mazzini, A., Etiope, G., 2017. Mud volcanism: An updated review: Earth-Science Reviews, 168, 81-112.
935 Menapace, W., Völker, D., Sahling, H., Zoellner, C., dos Santos Ferreira, C., Bohrmann, G., & Kopf, A. (2017).
936 Long-term in situ observations at the Athina mud volcano, Eastern Mediterranean: Taking the pulse of mud
937 volcanism. Tectonophysics, 721, 12-27.

938 Menapace, W., Tangunan, D., Maas, M., Williams, T., & Kopf, A. (2019). Rheology and biostratigraphy of the
939 Mariana serpentine muds unravel mud volcano evolution. Journal of Geophysical Research: Solid Earth,
940 124(11), 10752-10776.
941 Miller, C. A., Williams-Jones, G., Fournier, D., Witter, J., 2017. 3D gravity inversion and thermodynamic
942 modelling reveal properties of shallow silicic magma reservoir beneath Laguna del Maule, Chile, Earth and
943 Planetary Science Letters, 459, 14-27. http://dx.doi.org/10.1016/j.epsl.2016.11.007
944 Mellors, R., Kilb, D., Aliyev, A., Gasanov, A., Yetirmishli, G., 2007. Correlations between earthquakes and large
945 mud volcanoes eruptions. Journal of Geophysical research, 112, B04304. doi:10.1029/2006JB004489.
946 Odonne, F., Ménard, I., Massonnat, G. J., Rolando, J.-P., 1999. Abnormal reverse faulting above a depleting
947 reservoir. Geology, 27, 111-114.
948 Odonne, F., Imbert, P., Dupuis, M., Aliyev, A. A., Abbasov, O. R., Baloglanov, E. E., Vendeville, B. C., Gabalda,
949 G., Remy, D., Bichaud, V., Juste, R., Pain, M., Blouin, A., Dofal, A., Gertauda, M.. 2020. Mud volcano
950 growth by radial expansion: Examples from onshore Azerbaijan. Marine and Petroleum Geology
951 112,104051.
952 Praeg, D., Ceramicola, S., Barbieri, R., Unnithan, V., Wardell, N., 2009. Tectonically-driven mud volcanism since
953 the late Pliocene on the Calabrian accretionary prism, central Mediterranean Sea. Marine and Petroleum
954 Geology, 26, 1849-1865. doi:10.1016/j.marpetgeo.2009.03.008.
955 Planke, S., Svensen, H., Hovland M., Banks, D. A., Jamtveit, B., 2003. Mud and fluid migration in active mud
956 volcanoes in Azerbaijan. Geo-Mar. Letters, 23, 258-268. https://doi: 10.1007/s00367-003-0152-z
957 Ramsay, J. G., 1967. Folding and Fracturing of Rocks. Mc Graw Hill, New York, 568p.
958 Roberts, K. S., Davies R. J., Stewart S. A., 2010. Structure of exhumed mud volcano feeder complexes, Azerbaijan.
959 Basin Research, 22, 439-451.
960 Roberts, K. S., Davies R. J., Stewart S. A., Tingay, M., 2011. Structural controls on mud volcano vent distributions:
961 examples from Azerbaijan and Lusi, east Java. Journal of the Geological Society, London, 168, 1013-1030.
962 https://doi: 10.1144/0016-76492010-158.
963 Roche, O., Druitt, T. H., Merle, O., 2000. Experimental study of caldera formation. Journal of Geophysical
964 Research, 105, B1, 395-416.
965 Rosen, P. A., Gurrola, E., Sacco, G. F., Zebker, H., 2012. The InSAR Scientific Computing Environment.

966 Rudolph, M. L., Karlstrom, L., & Manga, M. (2011). A prediction of the longevity of the Lusi mud eruption,
967 Indonesia. Earth and Planetary Science Letters, 308(1-2), 124-130.
968 Scandone, R., 1990. Chaotic collapse of calderas. Journal of Volcanology and Geothermal Research, 42, 285-302.
969 Smith-Rouch, L. S., 2006. Oligocene-Miocene Maykop/Diatom total petroleum system of the South Caspian Basin
970 province, Azerbaijan, Iran, and Turkmenistan. U. S. Geological Survey Bulletin, 2201, 1-27.
971 Somoza, L., Medialdea, T., León, R., Ercilla, G., Vázquez, J. T., Farran, M.-L., Hernández-Molina, J., González,
972 J., Juan, C., Fernández-Puga, C., 2012. Structure of mud volcano systems and pockmarks in the region of
973 the Ceuta Contourite Depositional System (Western Alborán Sea). Marine Geology, 332-334, 4-26.
974 http://dx.doi.org/10.1016/j.margeo.2012.06.002
975 Stewart, S. A., Davies, R. J., 2006. Structure and emplacement of mud volcano systems in the South Caspian
976 Basin: AAPG Bulletin, 90, 771-786. https://doi:10.1306/11220505045
977 Tadono, T., Nagai, H., Ishida, H., Oda, F., Naito, S., Minakawa, K., a, Iwamoto, H., 2016. Generation of the 30
978 m-mesh global digital surface model by ALOS prism. The International Archives of the Photogrammetry,
979 Remote Sensing and Spatial Information Sciences, Volume XLI-B4, 2016 XXIII ISPRS Congress, 12–19
980 July 2016, Prague, Czech Republic.
981 Troll, V. R., Walter, T. R., Schmincke, H.-U., 2002. Cyclic caldera collapse: Piston or piecemeal subsidence?
982 Field and experimental evidence. Geology, 30, 135-138.
983 Tscherning, C. C., Forsberg, R., Knudsen, P., 1992. The GRAVSOFT package for geoid determination. Proc. 1.
984 Continental Workshop on the Geoid in Europe, Prague, May 1992, pp. 327–334. Research Institute of
985 Geodesy, Topography and Cartography, Prague.
986 Vincent, S. J., Allen, M. B., Ismail-Zadeh, A. D., Flecker, R., Foland, K. A., Simmons, M. D., 2005. Insights from
987 the Talysh of Azerbaijan into the Paleogene evolution of the South Caspian region: GSA Bulletin, 117,
988 1513-1533. https://doi: 10.1130/B25690.1
989 Viola, G., Andreoli, M., Ben-Avraham, Z., Stengel, I., Reshef, M., 2005. Offshore mud volcanoes and onland
990 faulting in southwestern Africa: neotectonic implications and constraints on the regional stress field. Earth
991 and Planetary Science Letters, 231, 147-160. https://doi:10.1016/j.epsl.2004.12.001
992 Wright, T., Parson, B., Zhong, L., 2004. Toward mapping surface deformation in three dimension using InSAR.
993 Geophysical Research Letters doi:10.1029/2003GL018827.

994 Yusifov, M., Rabinowitz, Ph. D., 2004. Classification of mud volcanoes in the South Caspian Basin, offshore
995 Azerbaijan: Marine and Petroleum Geology, 21, 965-975. https://doi:10.1016/j.marpetgeo.2004.06.002
996
997
998
999 **Figure captions**
1000
1001 Figure 1. a) Part of DEM of Azerbaijan processed with QGIS software showing the position of the four
1002 studied mud volcanoes; b) Geological map of eastern Azerbaijan with Absheron Peninsula, redrawn
1003 from Alizadeh (2008); c) Summary stratigraphic log for the Kura and South Caspian Basins, modified
1004 from Javanshir et al. (2015) and Blouin et al (2019)
1005
1006 Figure 2. a) Photos of Toragay, a conical mud volcano, and Ayazakhtarma, an example of a flat volcano.
1007 b) satellite views (Google Earth) of the 4 studied mud volcanoes; color lines show the location of the
1008 topographic profiles in c); Scale bar in the lower left corner of the Otmanbozdag picture is 1500 m long,
1009 and applies to all four images; c) Topographic profiles (from Google Earth, vertical exaggeration x2) of
1010 the two conical and of the two flat mud volcanoes studied here. All topographic profiles are in the SW-
1011 NE direction. Note that the Google Earth topography of the Otmanbozdag MV predates the 2018
1012 eruption discussed in the text.
1013
1014 Figure 3. The Otmanbozdag MV. a) mosaic of drone photos taken in May 2019 showing the summit of
1015 the volcano with the outer edge of the caldera forming the crater rim, the deformed central mud pie in
1016 the crater, the emission center “C” of the 2018 eruption and the area of overflow to the south; dashed
1017 rectangles indicate the position of the close-ups in Fig. 3; b) photo taken on September 23, 2018 showing
1018 the eruption that formed the large flows to the south, note the flames at the top of the volcano.
1019

Figure 4. Detail of the rectangles drawn in Figure 3. a) outer border of the volcano showing the thrust of the mud pie towards the rim of the caldera (upper inset on the right) as well as the large extensive fractures that go around the crater (lower inset); b) western edge of the mud pie showing the tilted blocks passing to diamond-shaped structures towards the center as well as rafts in relief; c) area of overflow of the mud flows to the south, the channel sides collapsed and fractures surfaces show horizontal grooves at top which evolve to normal oblique grooves downward.

Figure 5. Comparison between pre-2018 DEM from ALOS and our GNSS data acquired after the September 2018 eruption. DEM data before the 2018 eruption (black dots on the transects) are 10 to 15 meters higher than GNSS measurements (red dots) in the central part of the caldera and roughly coincide close to the edges.. After deflation, the floor of the caldera is flat and close to horizontal.

Figure 6. Example interferograms and easting and vertical components of the displacement at the Otmanbozdag MV. In each figure, the black circular line corresponds to the rim of the summit caldera. a) Sentinel-1 wrapped interferograms for the pre-eruptive period. b). Sentinel-1 wrapped interferograms for the post-eruptive period. c) Ascending and descending Sentinel-1 and ALOS-2 wrapped interferograms encompassing the September 2018 eruption. Each fringe (full color cycle) represents 2.83 cm (Sentinel-1) or 11.81 cm (ALOS-2) of range change between the ground and the satellite. The satellite to ground radar line of sight is shown with black arrow. d) Easting and vertical components of the displacement observed during the eruption obtained from ALOS-2 data. Areas in grey correspond to low coherence areas or to areas characterized by unwrapping errors. Coordinates are expressed in UTM-WGS84 (39 zone North).

Figure 7. Bouguer anomaly maps at mud volcanoes surveyed in this study overlain onto the topographic map. Black and red dots show the locations of the gravity measurements acquired during two field surveys in May 2018 and 2019. a) Bouguer anomaly maps at Otmanbozdag and Toragay conical mud

volcanoes. Maximum negative gravity anomalies range from -1 mGal at Toragay MV to -3 mGal at Otmanbozdag MV. b) Bouguer anomaly maps at Ayazakhtarma and Akhtarma-Pashaly flat mud volcanoes. Maximum negative gravity anomalies of about -8 mGal are observed over both volcanoes. Red dots show for both volcanoes the location of the NW-SE and SW-NE transects of observed gravity measurements plotted in the right panels. The 520 m and the 275 m contour roughly coincide with the limit between the plateau and the flanks of the Ayazakhtarma MV and the Akhtarma-Pashaly MV, respectively.

Figure 8. Elevation and cross sections from the inversion model using a density contrast from 0.05 to -500 $kg.m^{-3}$. Blue dashed lines give the location of the elevation sections. The map conventions are the same as in Fig.6. In conical mud volcanoes, a limited mud volume can be detected at medium depth while a large but very shallow volume of mud corresponds to the large negative gravity anomaly of flat mud volcanoes.

Figure 9. Photos of the Toragay MV. a) seen from the south, we see the flat summit and the relief of 300 m; b) drone mosaic taken in May 2019 showing the summit and the flow towards the West; c) summit drone mosaic and line drawing of the pie-like mudflows and the caldera edge (yellow); c-1) opposing edges of the two pie-like mudflows in the center; c-2) NW edge of the caldera; c-3) western edge of the caldera pushed by the western mudflow; c-5) rim fault at the SE edge of the caldera offsetting a young pie-like mudflow; b-5) NE edge of the caldera stopping the progress of a young pie-like mudflow whose fresh mud is still affected by the collapse of the caldera.

Figure 10. Sentinel-1 InSAR time series of the Toragay. Co-eruptive interferograms show that deformation is limited to the top part of the mud volcano but the low coherence of the signal does not make it possible to specify the type of displacement during the eruptions. Only post eruptive

1071 interferograms of July 2018 show significant ground displacement patterns, which could be related to
1072 their progressive contraction through desiccation.
1073
1074 Figure 11. a) Akhtarma-Pashaly MV satellite view showing the plateau and ancient flows to the SW; b)
1075 drawing of the mud flows and plateau; c) topographic profile A-B with a vertical exaggeration of 4.4.
1076 High slope values are only observed in the upper apron.
1077
1078 Figure 12. Photos of the Akhtarma-Pashaly MV; a) general profile of the volcano whose flat summit is
1079 approximately 2 km across; b) Schematic line drawing of the plateau and the four pie-like mudflows; c)
1080 satellite picture of the central mud pie and its peripheral deformations; d) folds over a decollement
1081 surface; e) southern edge of the mud pie which is thrusted over the plateau to the south; the
1082 corresponding local bending of the plateau creates small elongate depressions filled by rainwater; f)
1083 eastern edge of the mud pie where the fresh mud has overflowed beyond the compressive structures.
1084
1085 Figure 13. a) Example Sentinel-1 interferograms at Akhtarma-Pashaly MV. Slow vertical positive and
1086 negative displacements are observed except in two cases (a-2 and a-4) where the loss of coherence is an
1087 indication of large displacement distributed all over the plateau; b) Easting and vertical components of
1088 the displacement observed from July 24 to Sept. 4, a double-lobe pattern characteristic of horizontal
1089 expansion is observed in b-1. The map conventions are the same as in Fig.6.
1090
1091 Figure 14. Ayazakhtarma MV; a) general view of the flat surface which measures almost 3 km in its
1092 greatest length; b) small arrows = displacement vectors traced from SPOT7 satellite images taken
1093 between October 2011 and December 2017 (Odonne et al., 2020); large block arrows are regionally
1094 averaged displacements over the same period with a 10 x enlargement c) small active thrust NE of the
1095 volcano; d) detail of the strike slip striae on the N edge of the small thrust.
1096

Figure 15. a) Subset of Sentinel-1 InSAR interferograms at Ayazakhtarma MV. High coherence of interferograms indicate an almost permanent and slow activity of the Ayazakhtarma MV during time intervals shown in a1-a2 and a4-a6, while an acceleration of displacement is observed in the center of the mud volcano during the time interval shown by a-3; b) Easting and vertical components of the displacement observed in June 2018 show a double-lobe pattern characteristic of horizontal expansion (b-1). The map conventions are the same as in Fig.6.

Figure 16. Kinematic model of the development of the Otmanbozdag structures before and after the September 2018 eruption; a) swelling of the central mud pie which is progressively thrusted over the peripheral moat of the caldera; b) beginning of the September 2018 eruption, the central mud pie begins to breach the southern edge of the caldera; c) main eruption phase with the flows draining a large volume of the mud from the central dome, the latter collapsing with large extensional structures; d) interpreted section of the mud volcano with two mud chambers, an upper one a few meters below the surface having emitted part of its content during the 2018 eruption (mudflow to the south) and a deeper one whose depth is controlled by gravity modeling and geometric constraints (see text for details). The red dashed line indicates the pre-eruption topography of the dome.

Figure 17. Kinematic model of the Toragay MV; a) pre-2018 morphology: December 12, 2016 Google Earth image of the summit of Toragay with in overlay a line drawing of the the edge of the caldera (yellow) and the outline of old pie-like mudflows (black); green patches are episodic small lakes b) post-2018 eruption morphology: drone mosaic acquired in May 2019 with in overlay line drawing of the three pie-like mudflows emitted in 2018 and their emission centers (stars); c) interpreted cross-section of the volcano along the 2018 mudflow on the western side; the position and volume of the mud chamber (purple) are derived from the gravity model.

Figure 18. Kinematic model of formation of flat volcanoes; a) oblique perspective sketch of the Ayazakhtarma MV showing the central emission zone, the middle ring with strike slip structures and pop up blocks and the compressive border wedge; b) oblique perspective sketch of the Akhtarma-Pashaly MV showing the flat plateau, the various small mud pies which are emission zones with bombs of mud and the outer edge in compression; c) proposed section of a generic flat volcano showing a large surface mud chamber spreading out towards the edge of the volcano where it forms a compressive wedge; d) detail of the compressive wedge (Dahlen, 1984) showing the tilting of the thrusts, back-thrusts and therefore of $\sigma 1$. The inclination of the prism surface (8°) leads us to propose a slightly inclined base (2°).

Table 1. Slopes of thrusts and back-thrusts measured around the Akhtarma-Pashaly and the Ayazakhtarma mud volcanoes.

Table 1.

Akhtarma-Pashaly MV		Ayazakhtarma MV	
Thrusts (°)	Backthrusts (°)	Thrusts (°)	Backthrusts (°)
33	25	30	58
43	43	41	58
15	78	52	59
72	42	37	61
15		30	56
30		78	51
20		60	65
20		21	
75		15	
		23	
		58	
		76	

We compare the growth patterns of conical and flat mud volcanoes from Azerbaijan.

The comparison of structural field data, microgravimetry modeling and InSAR data highlights subsurface differences between flat and conical mud volcanoes.

Flat mud volcanoes develop by radial expansion and conical ones by stacking of mudpies in the crater and of radial flows on the flanks.

We evidence mud chambers from gravity data and delineate them from surface caldera.

We estimate the average depth and volume of mud chambers from the modeling of microgravity data.

Declaration of interests

☒The authors declare that they have no known competing financial interests or personal relationships that could have appeared to influence the work reported in this paper.

☐The authors declare the following financial interests/personal relationships which may be considered as potential competing interests:

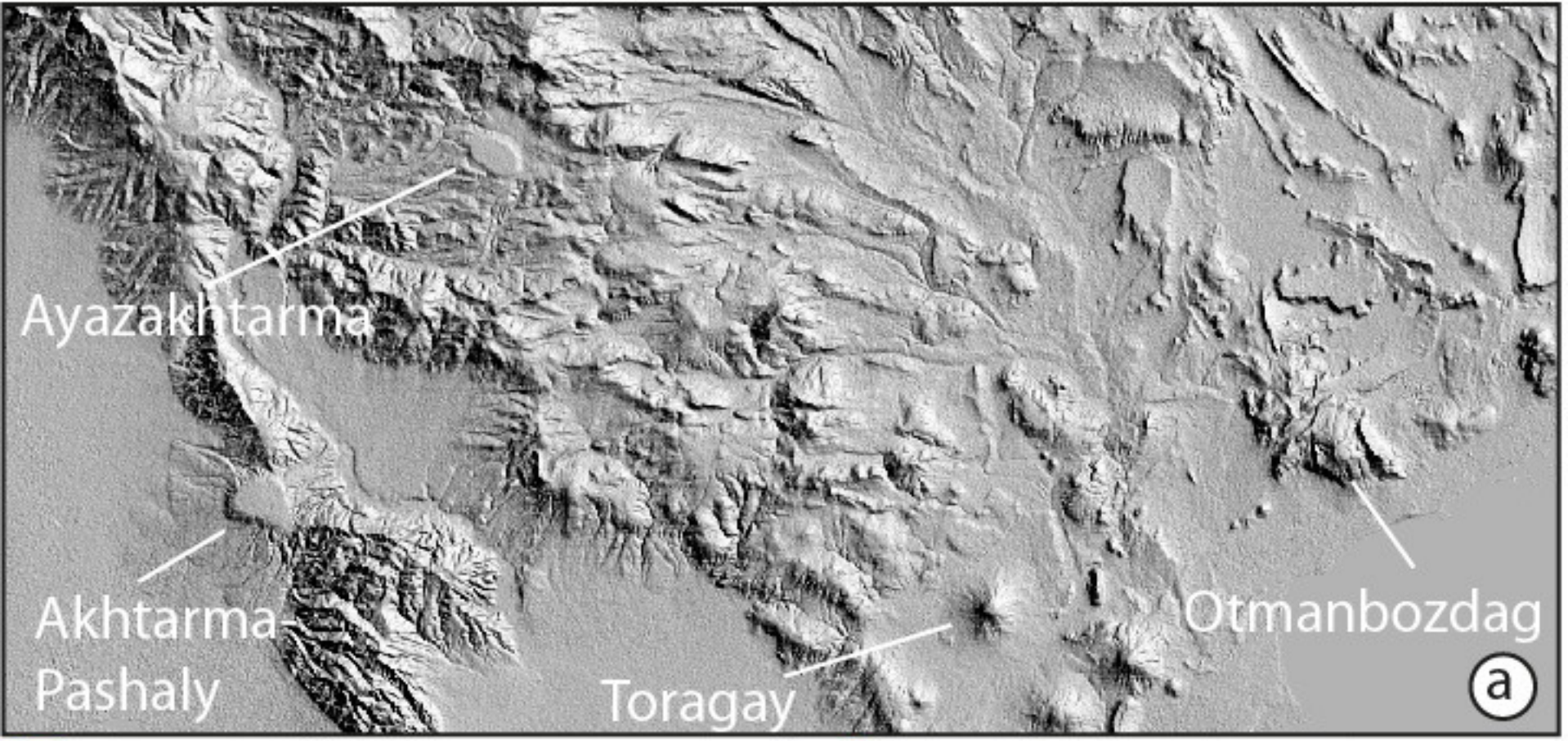
Ayazakhtarma
Akhtarma-
Pashaly
Toragay
Otmanbozdag
a

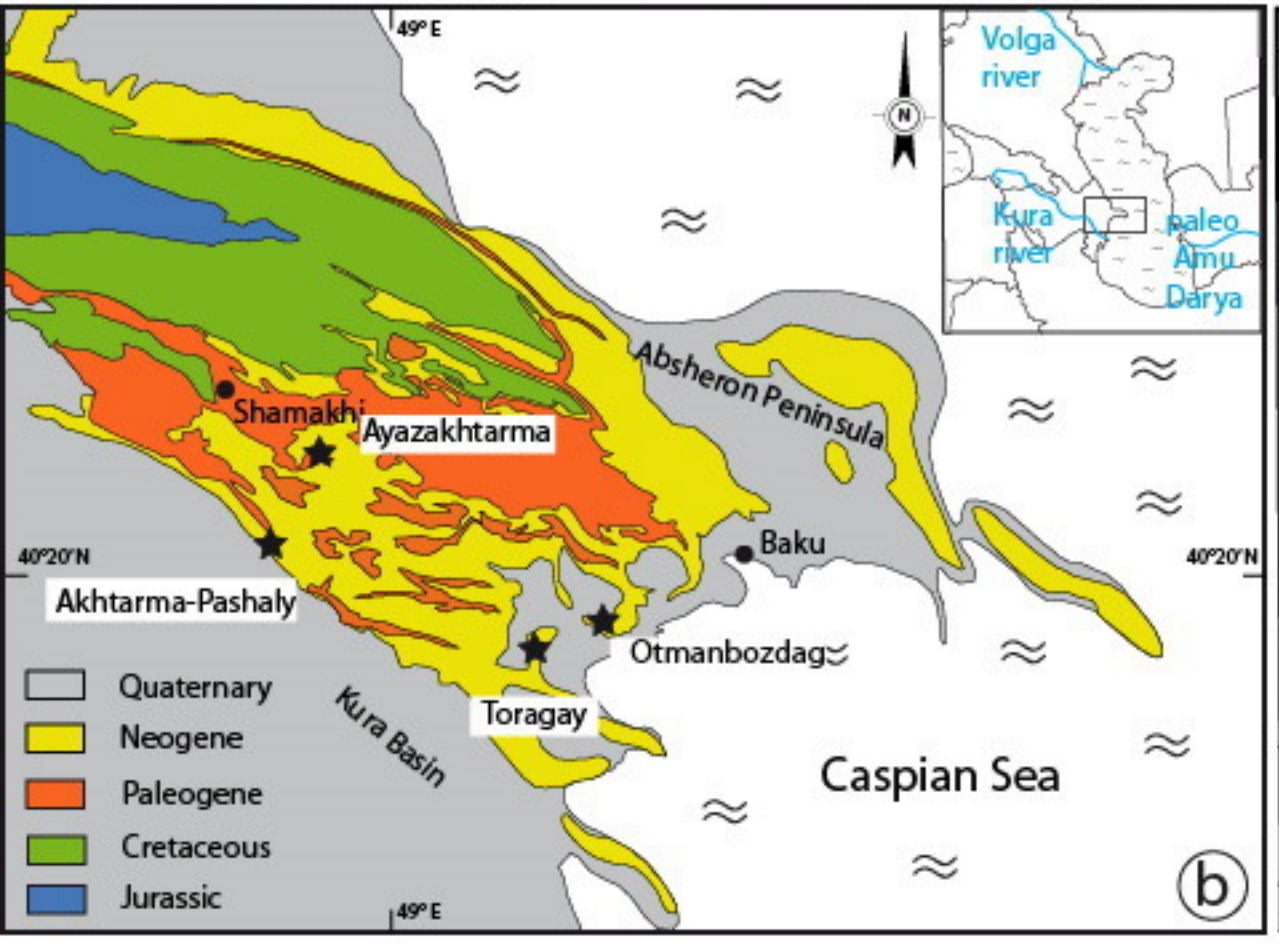
49° E
40°20'N
Volga
river
Kura
river
paleo
Amu
Darya
Absheron Peninsula
Shamakhi
Ayazakhtarma
Baku
Akhtarma-Pashaly
Otmanbozdag
Toragay
Kura Basin
Caspian Sea
Quaternary
Neogene
Paleogene
Cretaceous
Jurassic
b

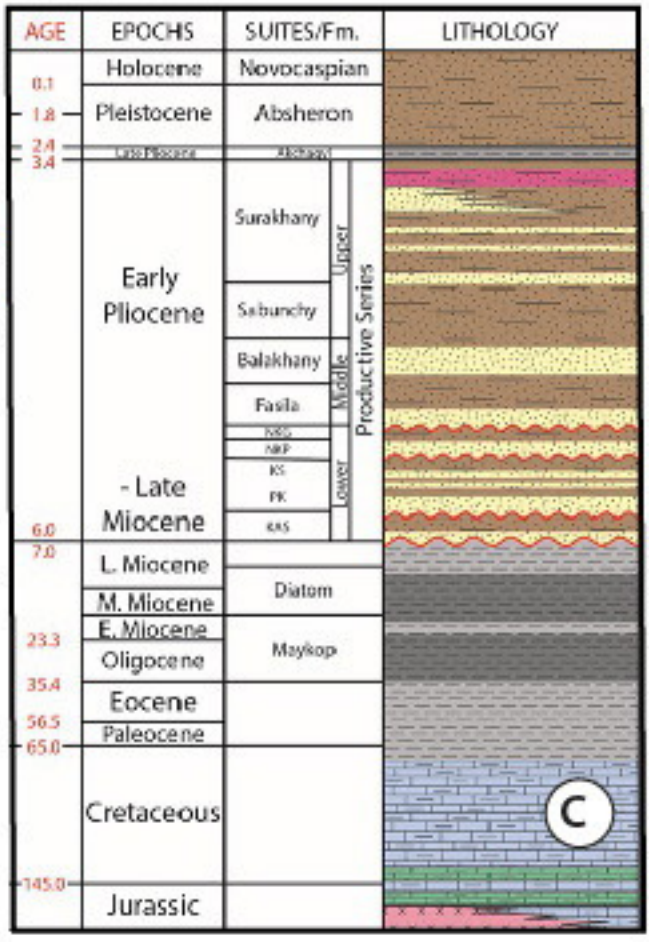
AGE
EPOCHS
SUITES/Fm.
LITHOLOGY
Holocene
Novocaspian
Pleistocene
Absheron
Early
Pliocene
- Late
Miocene
Surakhany
Sabunchy
Balakhany
Fasila
Upper
Middle
Lower
Productive Series
L. Miocene
M. Miocene
E. Miocene
Oligocene
Eocene
Paleocene
Cretaceous
Jurassic
Diatom
Maykop
0.1
1.8
2.4
3.4
6.0
7.0
23.3
35.4
56.5
65.0
145.0
c

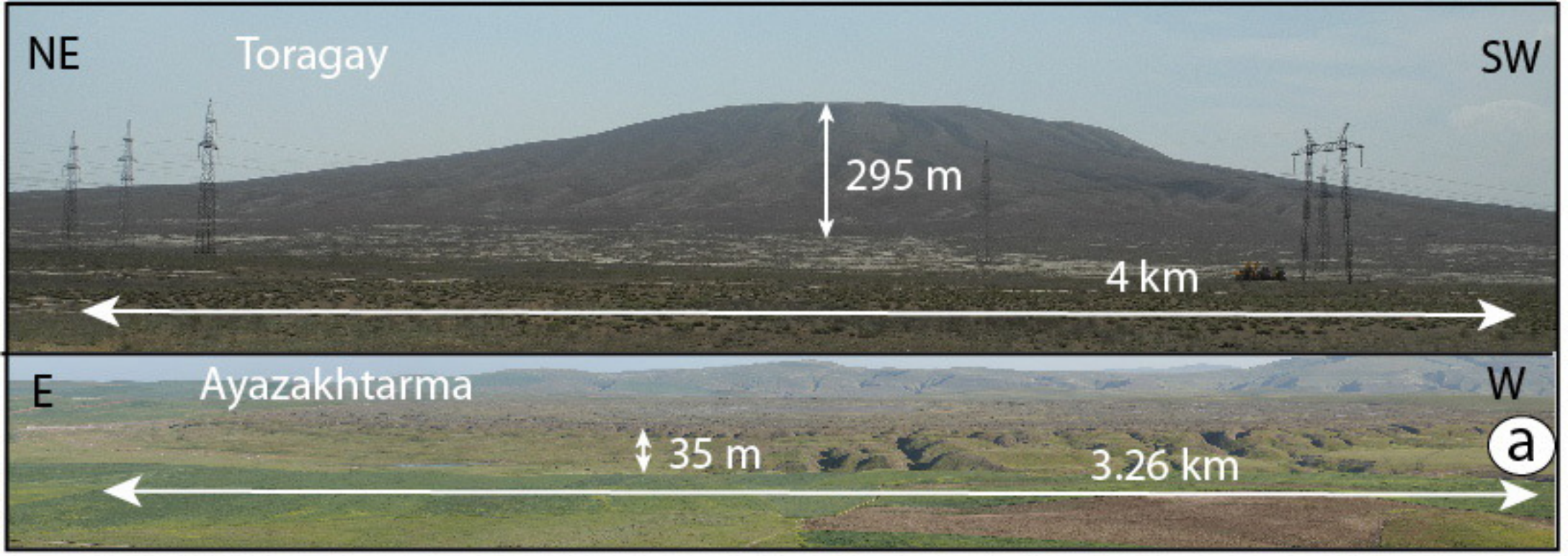
NE
Toragay
SW
295 m
4 km
E
Ayazakhtarma
W
35 m
3.26 km
a

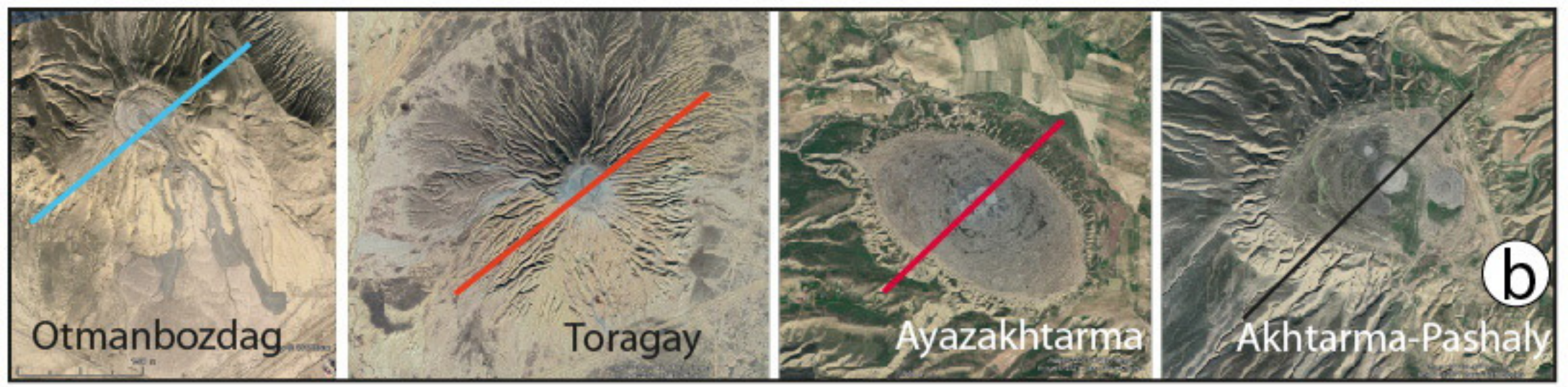
Otmanbozdag
Toragay
Ayazakhtarma
Akhtarma-Pashaly
b

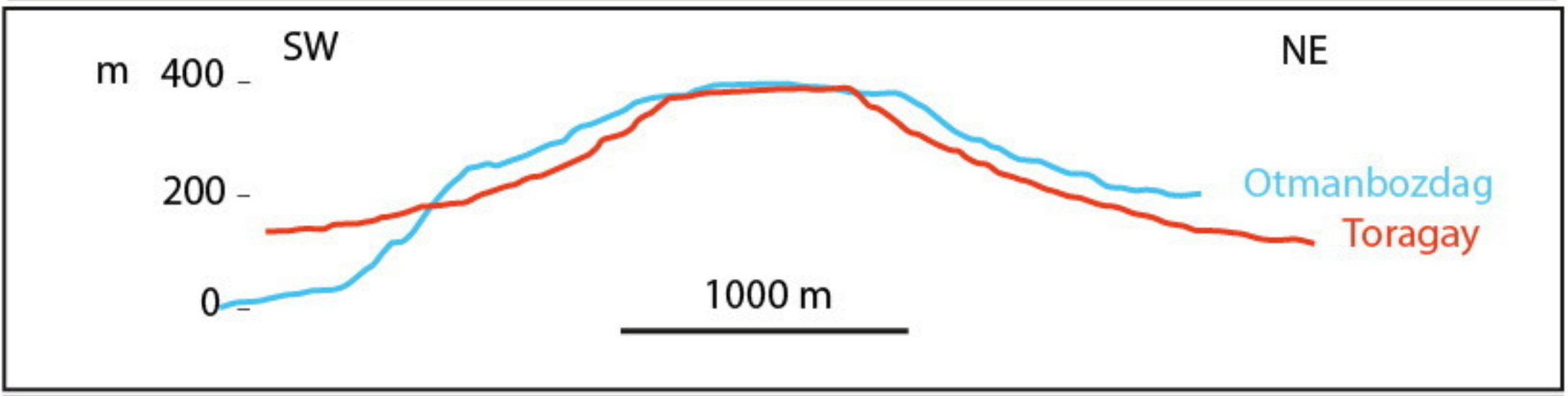
m
400
200
0
SW
NE
Otmanbozdag
Toragay
1000 m

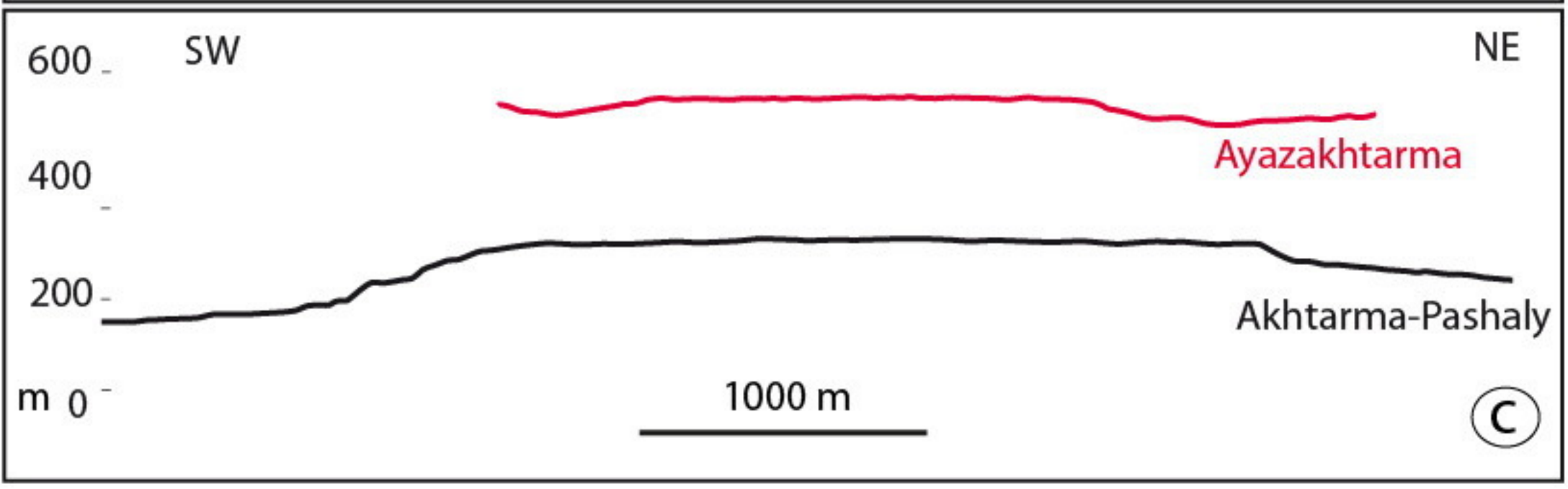
600
400
200
m 0
SW
NE
Ayazakhtarma
Akhtarma-Pashaly
1000 m
c

a

b

Crater rim

Fig. 4 a

Crater

Fig. 4 b

Fig. 4 c

2018 emission center (C)

N

40° 14′ 20″ N

Area of overflow

mudflows

500 m

49° 30′ 35″ E

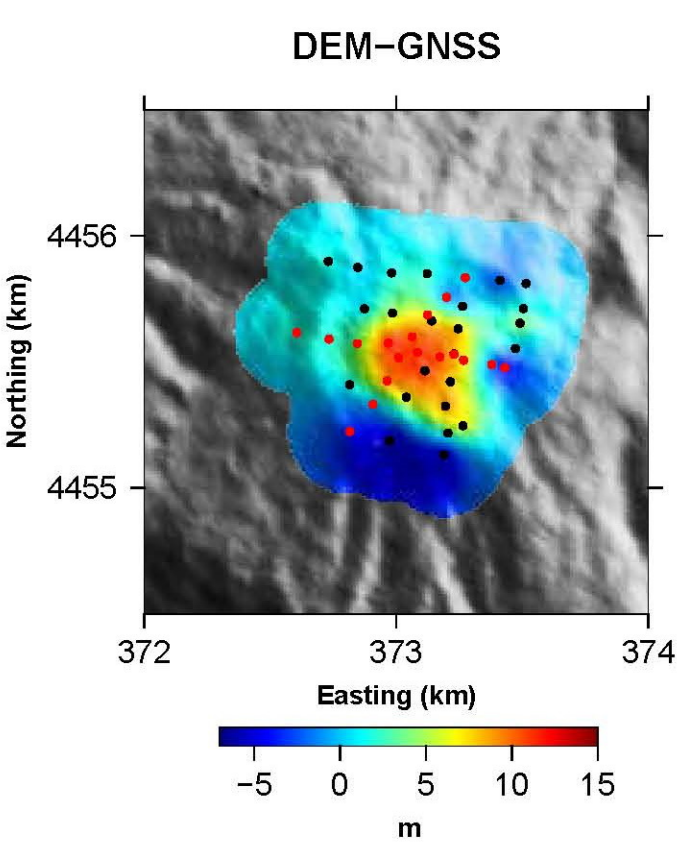
DEM−GNSS
4456
4455
Northing (km)
372
373
374
Easting (km)
−5
0
5
10
15
m

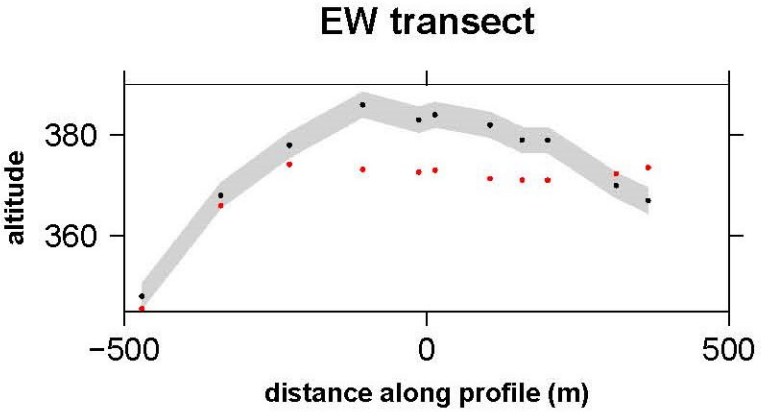
EW transect
380
360
altitude
−500
0
500
distance along profile (m)

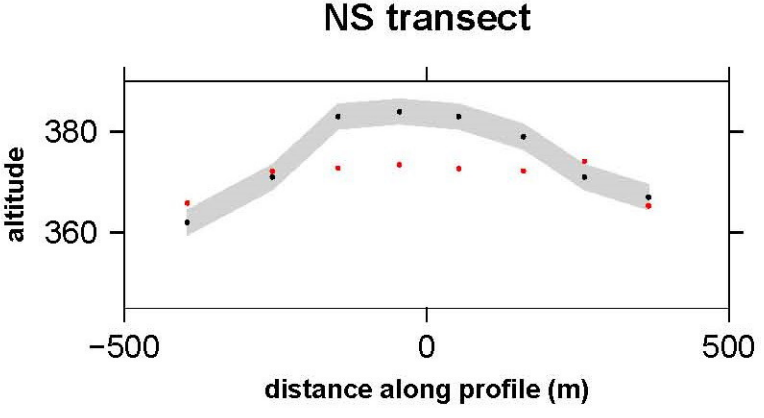
NS transect
380
360
altitude
−500
0
500
distance along profile (m)

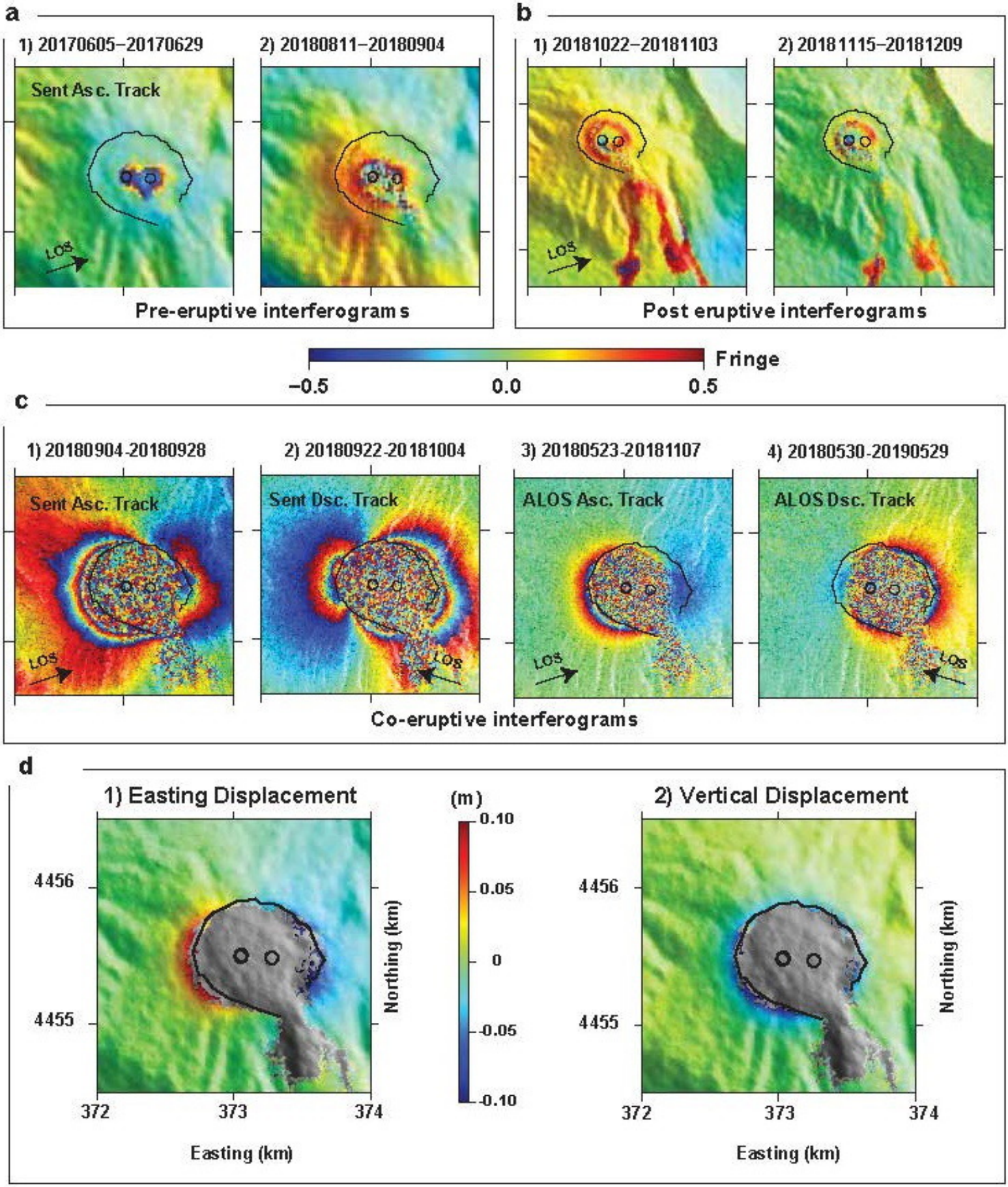
a
1) 20170605–20170629
2) 20180811–20180904
Sent Asc. Track
LOS
Pre-eruptive interferograms
b
1) 20181022–20181103
2) 20181115–20181209
LOS
Post eruptive interferograms
Fringe
−0.5
0.0
0.5
c
1) 20180904-20180928
2) 20180922-20181004
3) 20180523-20181107
4) 20180530-20190529
Sent Asc. Track
Sent Dsc. Track
ALOS Asc. Track
ALOS Dsc. Track
LOS
Co-eruptive interferograms
d
1) Easting Displacement
2) Vertical Displacement
(m)
0.10
0.05
0
-0.05
-0.10
4456
4455
Northing (km)
372
373
374
Easting (km)

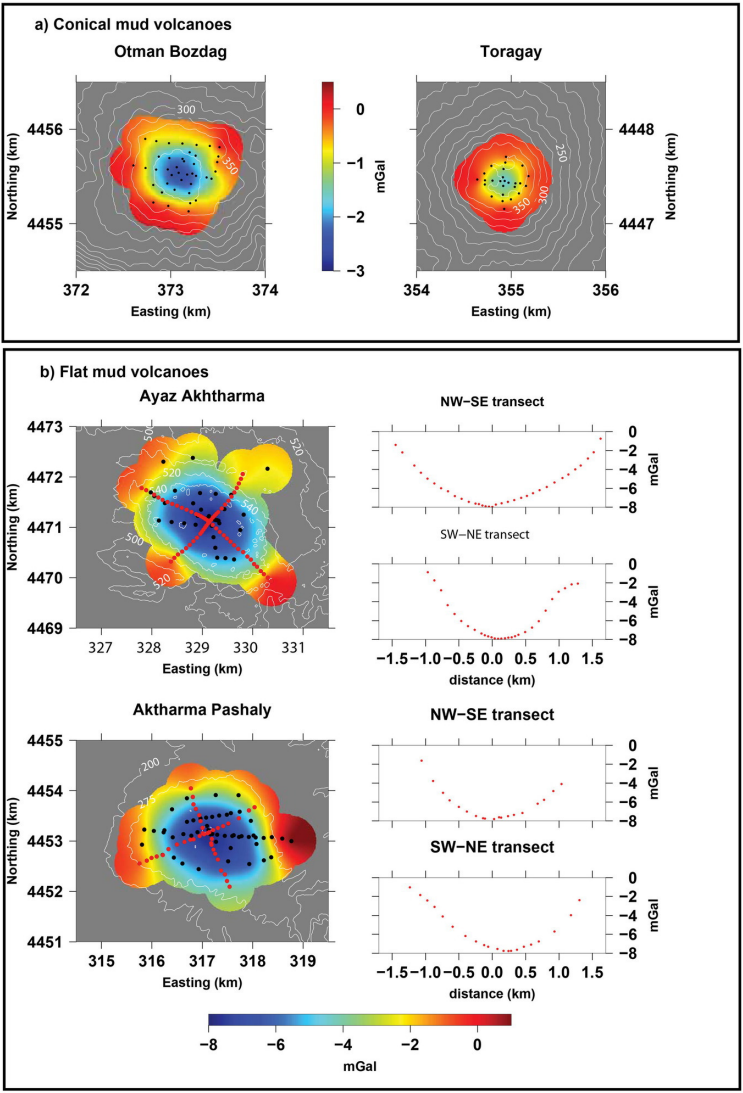
a) Conical mud volcanoes
Otman Bozdag
Toragay
Northing (km)
Easting (km)
mGal
b) Flat mud volcanoes
Ayaz Akhtharma
Aktharma Pashaly
NW–SE transect
SW–NE transect
distance (km)

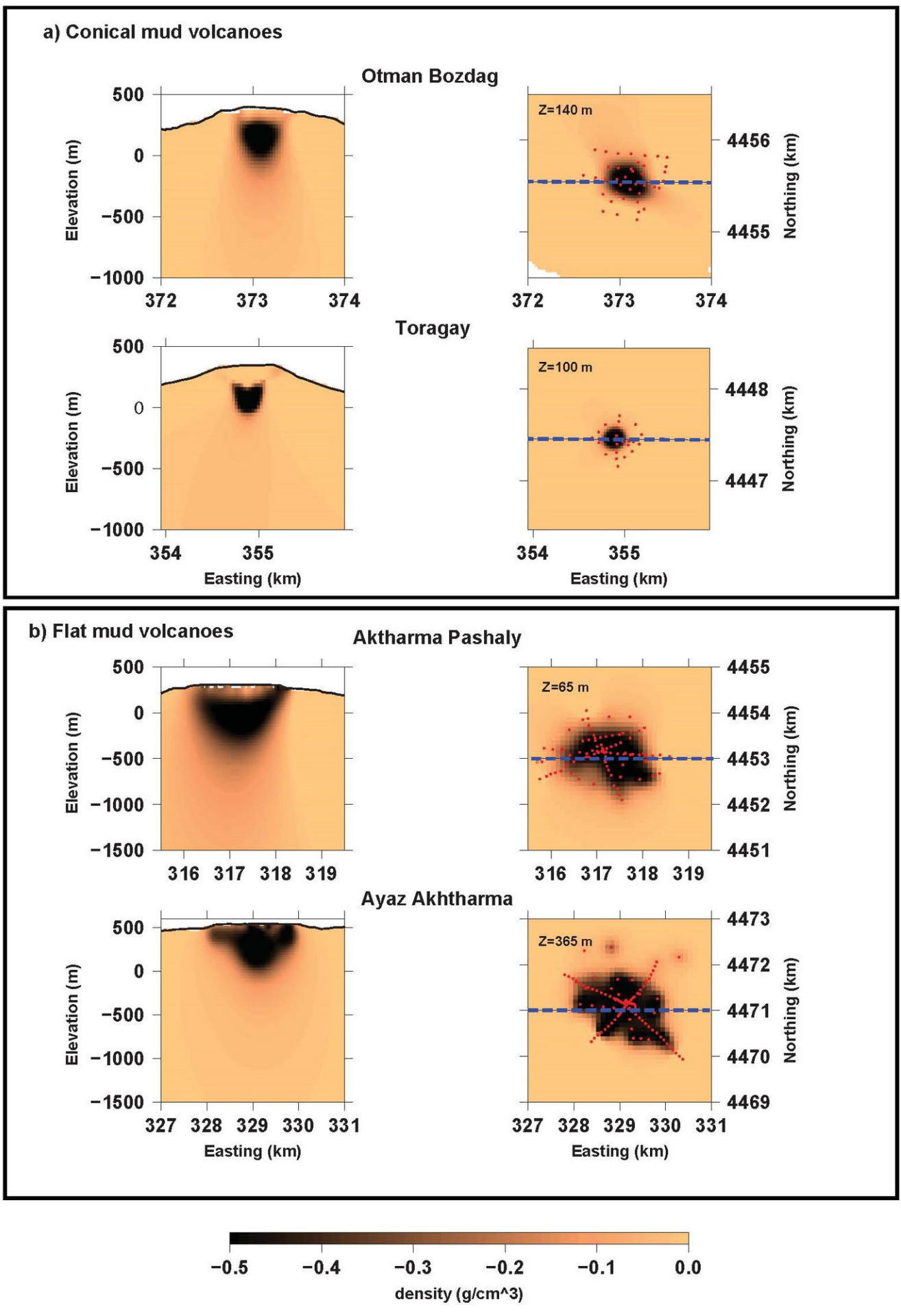
a) Conical mud volcanoes
Otman Bozdag
Elevation (m)
500
0
−500
−1000
372
373
374
Z=140 m
4456
4455
Northing (km)
Toragay
Elevation (m)
500
0
−500
−1000
354
355
Easting (km)
Z=100 m
4448
4447
Northing (km)
b) Flat mud volcanoes
Aktharma Pashaly
Elevation (m)
500
0
−500
−1000
−1500
316
317
318
319
Z=65 m
4455
4454
4453
4452
4451
Northing (km)
Ayaz Akhtharma
Elevation (m)
500
0
−500
−1000
−1500
327
328
329
330
331
Easting (km)
Z=365 m
4473
4472
4471
4470
4469
Northing (km)
−0.5
−0.4
−0.3
−0.2
−0.1
0.0
density (g/cm^3)

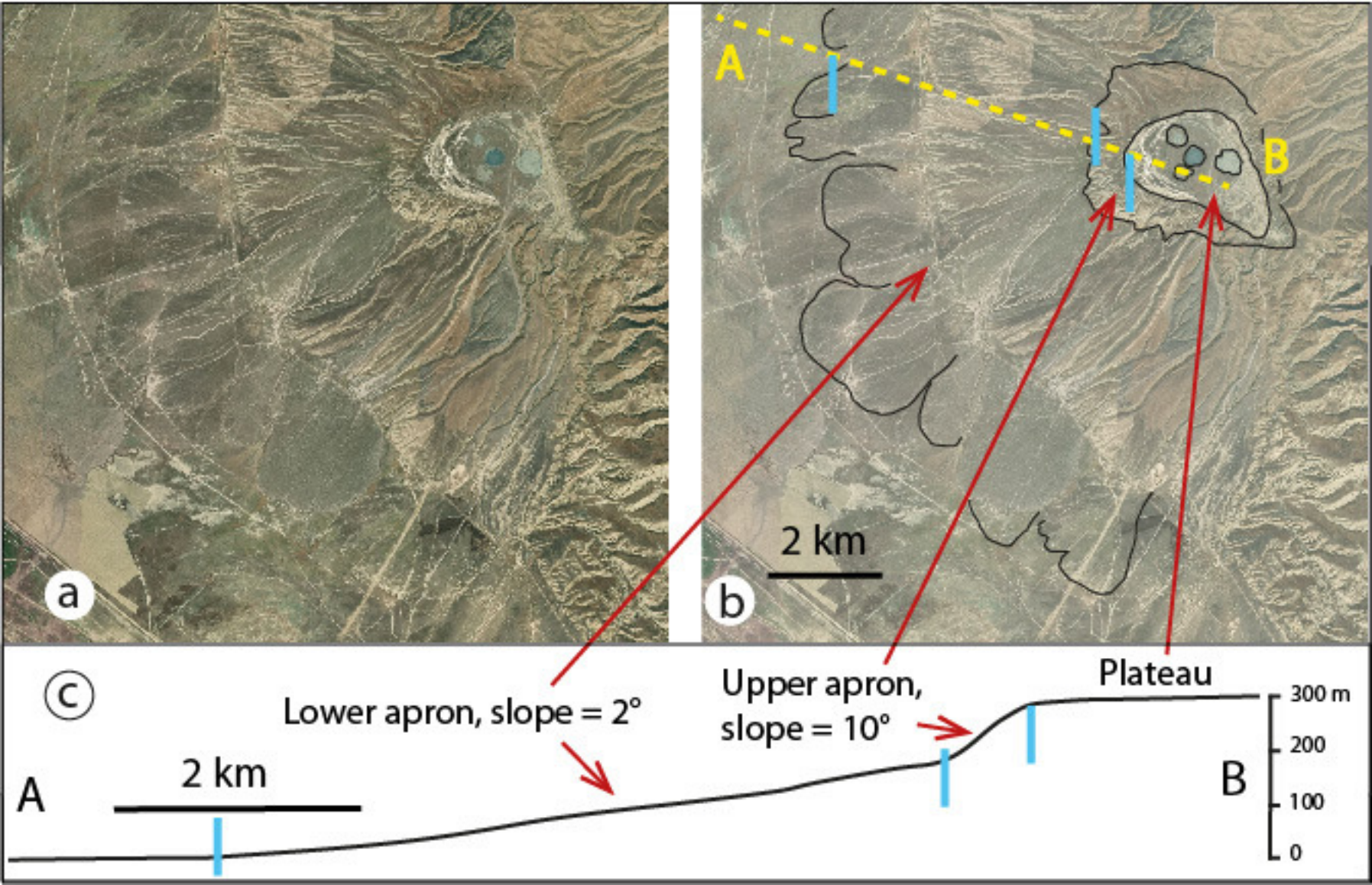
a
b
A
B
2 km
c
Lower apron, slope = 2°
Upper apron,
slope = 10°
Plateau
A
2 km
B
300 m
200
100
0

E

W

a

500 m

b

300 m

150

0

0

2500

5000

7500 m

40° 13′N

48° 51′E

N

40° 13′N

c

40° 12′N

48° 51′E

500 m

40° 12′N

d

N

40° 12′ 32″ N

100 m

48° 51′ 04″ E

SW

NE

g

5 m

NE

SW

e

2 m

SW

NE

f

5 m

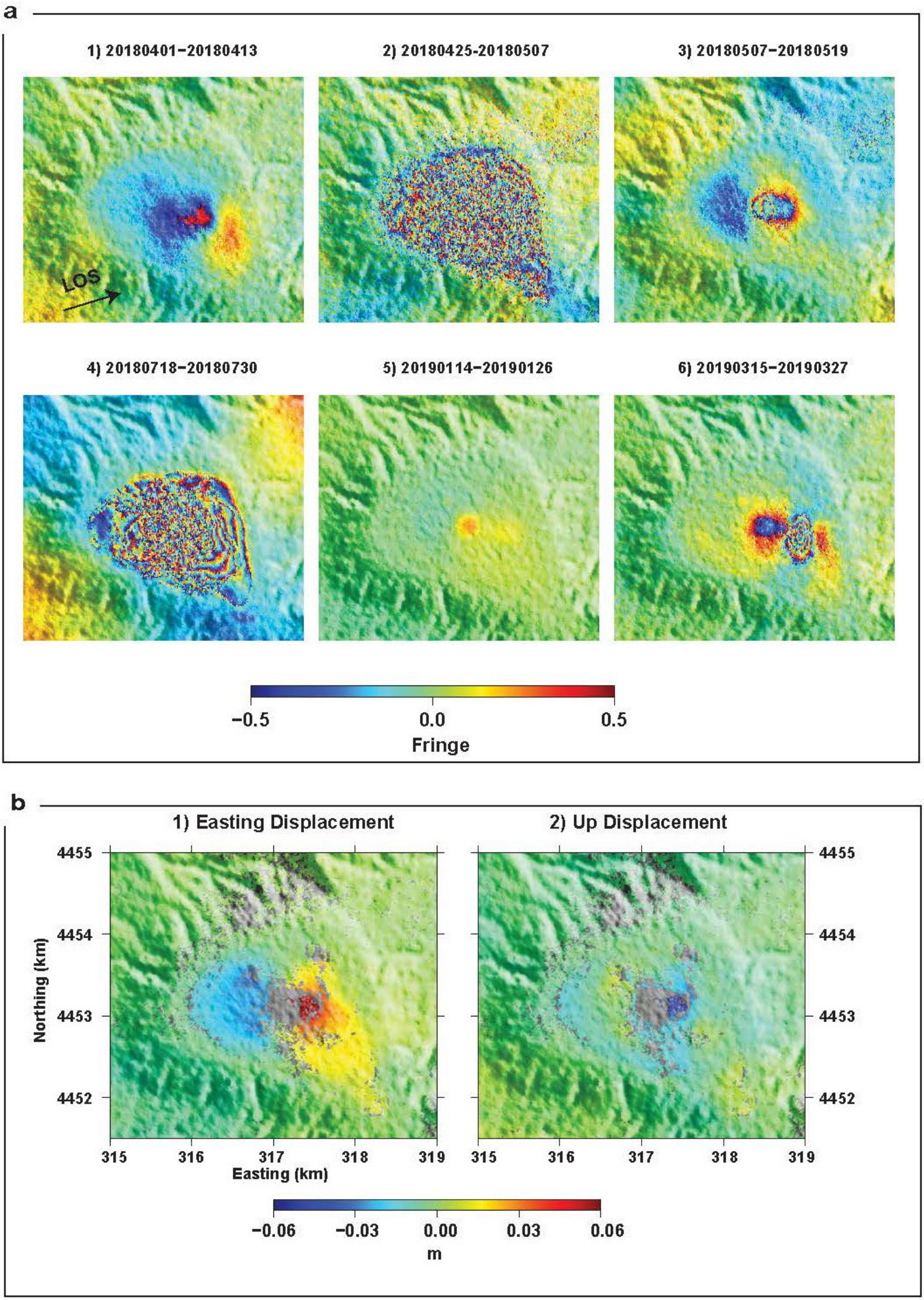
a
1) 20180401–20180413
2) 20180425-20180507
3) 20180507–20180519
LOS
4) 20180718–20180730
5) 20190114–20190126
6) 20190315–20190327
−0.5
0.0
0.5
Fringe
b
1) Easting Displacement
2) Up Displacement
4455
4454
4453
4452
Northing (km)
315
316
317
318
319
Easting (km)
−0.06
−0.03
0.00
0.03
0.06
m

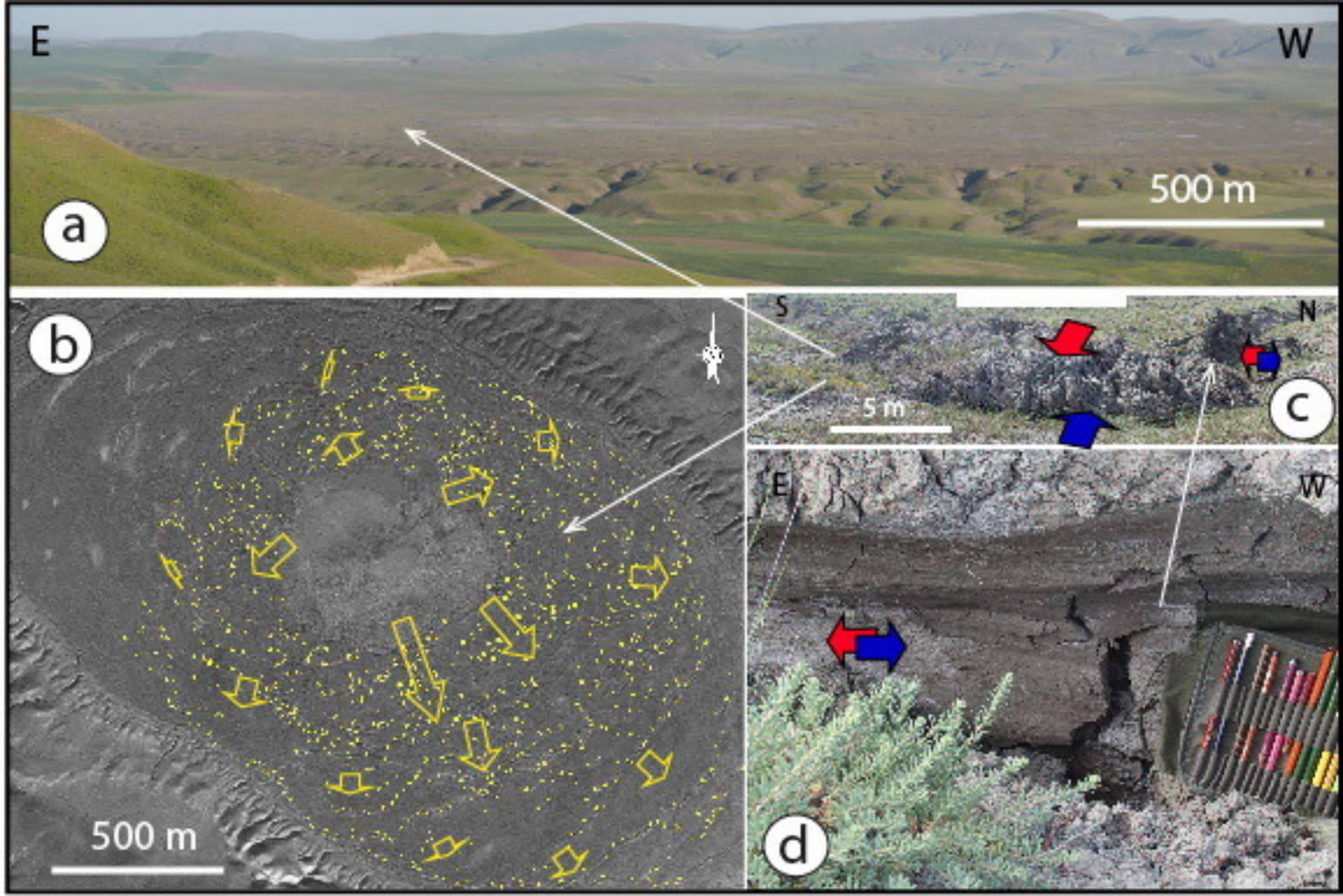
E
W
500 m
a
b
500 m
S
N
5 m
c
E
W
d

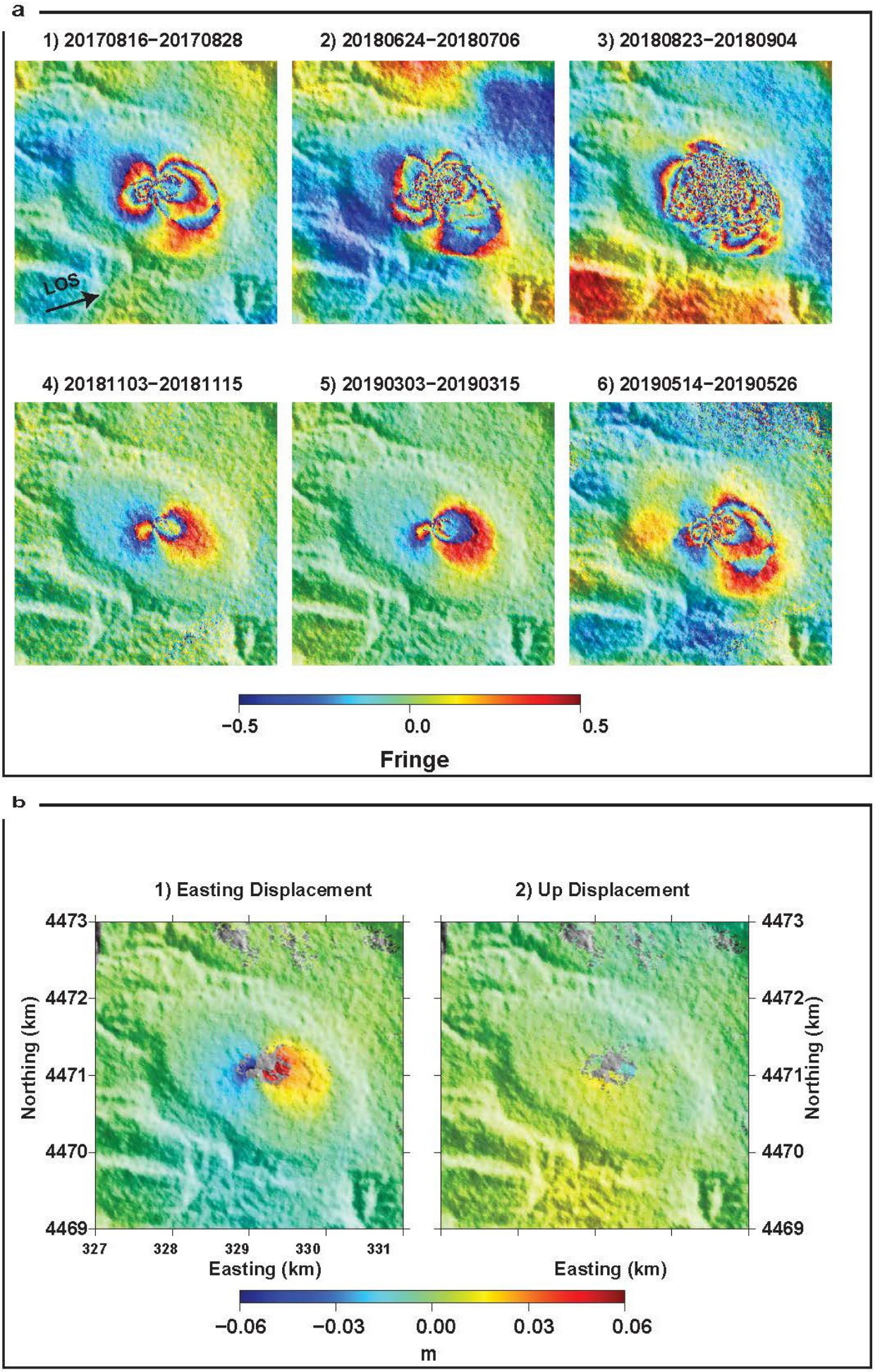
a
1) 20170816–20170828
2) 20180624–20180706
3) 20180823–20180904
LOS
4) 20181103–20181115
5) 20190303–20190315
6) 20190514–20190526
−0.5
0.0
0.5
Fringe
b
1) Easting Displacement
2) Up Displacement
4473
4472
4471
4470
4469
Northing (km)
327
328
329
330
331
Easting (km)
−0.06
−0.03
0.00
0.03
0.06
m